

# Optical BEAMTAP beam-forming and jammer-nulling system for broadband phased-array antennas

Gregory Kriehn, Andrew Kiruluta, Paulo E. X. Silveira, Sam Weaver, Shawn Kraut, Kelvin Wagner, R. Ted Weverka, and Lloyd Griffiths

We present an approach to receive-mode broadband beam forming and jammer nulling for large adaptive antenna arrays as well as its efficient and compact optical implementation. This broadband efficient adaptive method for true-time-delay array processing (BEAMTAP) algorithm decreases the number of tapped delay lines required for processing an  $N$ -element phased-array antenna from  $N$  to only 2, producing an enormous savings in delay-line hardware (especially for large broadband arrays) while still providing the full  $NM$  degrees of freedom of a conventional  $N$ -element time-delay-and-sum beam former that requires  $N$  tapped delay lines with  $M$  taps each. This allows the system to adapt fully and optimally to an arbitrarily complex spatiotemporal signal environment that can contain broadband signals of interest, as well as interference sources and narrow-band and broadband jammers—all of which can arrive from arbitrary angles onto an arbitrarily shaped array—thus enabling a variety of applications in radar, sonar, and communication. This algorithm is an excellent match with the capabilities of radio frequency (rf) photonic systems, as it uses a coherent optically modulated fiber-optic feed network, gratings in a photorefractive crystal as adaptive weights, a traveling-wave detector for generating time delay, and an acousto-optic device to control weight adaptation. Because the number of available adaptive coefficients in a photorefractive crystal is as large as  $10^9$ , these photonic systems can adaptively control arbitrarily large one- or two-dimensional antenna arrays that are well beyond the capabilities of conventional rf and real-time digital signal processing techniques or alternative photonic techniques.

© 2000 Optical Society of America

OCIS codes: 070.1060, 190.5330.

## 1. Introduction

Conventional broadband time-domain beam formers for antenna-array processing require one tapped delay line (TDL) for each antenna element to avoid beam squint, which is the undesired rotation of the angular receptivity pattern of the antenna with frequency. Often these TDL's are implemented with digital delay lines for narrow-band systems (up to a few megahertz of bandwidth). To process signals with a bandwidth up to  $\sim 1$  GHz, TDL's can be im-

plemented with ultrasonic delay lines, which can be conveniently tapped by acousto-optic (AO) diffraction.<sup>1</sup> At very high frequencies (perhaps even as great as 100 GHz) fiber-optic TDL's have been proposed.<sup>2-4</sup> Large arrays can have as many as 1000 elements for one-dimensional (1-D) arrays and as many as  $100 \times 100$  elements for two-dimensional (2-D) arrays, requiring  $N = 10^3$ – $10^4$  broadband TDL's, which is both expensive and technologically challenging. These TDL's are necessary for avoiding beam squint, which is especially troublesome in large arrays for large fractional bandwidth applications. To obtain squint-free octave-bandwidth beam forming over a half-space for a half-wavelength spaced array, each TDL needs at the minimum as many complex taps as there are elements in a 1-D phased array or elements along the longest diagonal for a 2-D array. Even more taps are required, however, for the equalization of antenna frequency response ripples, compensation for mutual coupling, or multipath processing.

To avoid the necessity for a large number of TDL's, many phased arrays are operated in a narrow-band

---

G. Kriehn (gregory.kriehn@colorado.edu), A. Kiruluta, P. E. X. Silveira, S. Weaver, S. Kraut, and K. Wagner are with the Optoelectronic Computing Systems Center, Department of Electrical and Computer Engineering, University of Colorado, Boulder, Colorado 80309-0425. R. T. Weverka is with Optoelectronic Data Systems, 232 Hacienda Street, San Mateo, California 94403. L. Griffiths is with the Engineering Department, George Mason University, Fairfax, Virginia 22030.

Received 24 May 1999; revised manuscript received 29 October 1999.

0003-6935/00/020212-19\$15.00/0

© 2000 Optical Society of America

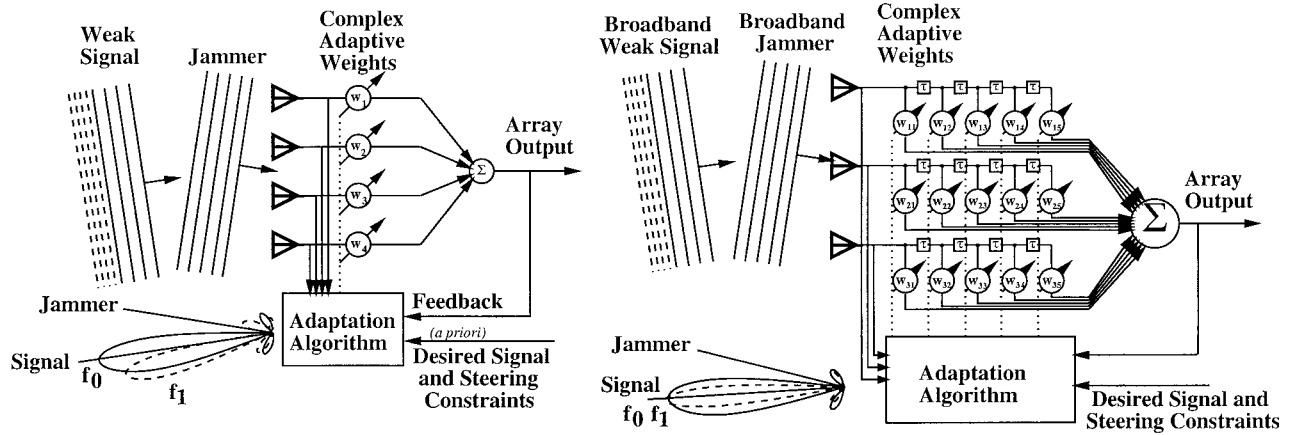


Fig. 1. (a) Narrow-band phased array that suffers from frequency-dependent beam squint. (b) Conventional broadband time-delay-and-sum beam-forming algorithm illustrating the requirement for one TDL at each antenna element to eliminate beam squint of the main beam and the nulls.

mode in which each antenna output is simply multiplied by a single complex coefficient for beam forming, as shown in Fig. 1(a). However, when the fractional bandwidth  $F = B/f_0$  (where  $B$  is the bandwidth and  $f_0$  is the center frequency) of a signal exceeds the spatial-array resolvability  $Q = \lambda_0/L \sin \theta_{\max}$  (where  $L$  is the maximum array aperture, which equals  $L = Nd$  for an  $N$ -element 1-D array of element spacing  $d$ ,  $\lambda_0 = c/f_0$ , and  $\theta_{\max}$  is the maximum angle from boresight over which the array must steer), then a plane-wave pulse arriving at a large angle  $\theta$  from boresight takes a time  $T = L/c \sin \theta$  to propagate across the array aperture, and this delay is resolvable within the bandwidth of the system. In this case, when  $F > Q$ , the antenna-array function is significantly altered as the frequency changes across the bandwidth  $B$ , resulting in an undesired angular rotation of the main beam and an additional undesired rotation of the nulls of the antenna pattern.

In current implementations of antenna beam formers when broadband operation is required (the condition in which  $F > Q$ ), a weighted TDL with at least  $M = \sin \theta_{\max} BL/c$  taps is required at every antenna element, as shown in Fig. 1(b). As an example, for a 1-D array with  $N = 1000$ , a center frequency of 2 GHz, a processing bandwidth of 1 GHz ( $F = 1/2$ ), a desired angular coverage from boresight to both end-fire directions ( $\theta_{\max} = 90^\circ$ ), with elements that are spaced at  $\lambda_m/2$  (where  $\lambda_m$  is the minimum detectable wavelength of the array),  $M = 200$  complex taps are required per array element. This results in a requirement of  $NM = 200,000$  complex taps for the entire 1-D array. For a  $100 \times 100$  2-D array operating at the same frequencies, 28 complex taps are required per antenna element, and a total of 280,000 complex taps are needed for beam forming without squint. In the alternative frequency-domain implementation, a temporal Fourier transform of each antenna output is implemented digitally with an array of  $N$  fast Fourier transform (FFT) modules and used to produce  $M = BL/c$  narrow-band systems, each of

which is steered with a straightforward complex multiplier operating at every antenna element at each resolvable frequency. After narrow-band beam forming is performed in each frequency bin, the desired broadband signal is reconstructed by an inverse FFT of the summed narrow-band outputs. However, the frequency-domain implementation ignores correlations between frequency components (i.e., it assumes an on-diagonal block Toeplitz correlation structure) that can produce erroneous results in certain broadband situations. In addition, this frequency-domain system has as many FFT modules as conventional time-domain beam formers have delay lines ( $N$ ), and the FFT modules are far more complex to implement than a delay line, especially for real-time operation.

In this paper we describe a novel, more efficient algorithm for broadband time-domain beam forming of arbitrarily large arrays that requires only one input TDL detector and one output TDL modulator for weight programming. This BEAMTAP [broadband efficient adaptive method for true-time-delay (TTD) array processing] system makes broadband beam forming viable for large arrays and is well matched to implement with radio frequency (rf) photonic hardware. In addition, BEAMTAP is compatible with the real-time calculation of the required  $MN = NF/Q$  adaptive weights that encompass the necessary degrees of freedom to nearly optimally beam steer and null rotate without squint in an arbitrarily complex spatiotemporal signal environment.

We begin by comparing the conventional time-domain beam former with the new hardware-efficient BEAMTAP architecture, and we show their mathematical equivalence before discussing the benefits and challenges of the proposed optical array processing system as compared with other photonic approaches and digital signal-processing implementations. Then the proposed rf photonic implementation with a fiber-remoted coherent phased array, photorefractive crystal, traveling-wave detector, and AO device (AOD) is

outlined. The details of the rf offset frequencies, grating recording, coherent interferometric detection, and closed-loop optical system operation are then derived in Section 3. Simulations are presented that demonstrate the operations of TTD main-beam forming and jammer nulling for far-field broadband signals. Finally, we conclude with a summary of our results.

## 2. Optical Phased-Array Radar Processing

There have been numerous approaches to optically implementing adaptive phased-array phase-only beam steering, all of which unfortunately suffer from beam squint for broadband signals.<sup>5,6</sup> Previous optical implementations of broadband adaptive beam forming<sup>7–11</sup> avoided beam squint by use of multichannel AO delay lines to implement a TDL for every antenna element input, but are limited to 32–64 channels because of the limits of AO technology.<sup>12</sup> Fiber-optic TTD beam-forming networks have been employed to bring the main beam onto the apparent array boresight where there is no frequency-dependent beam squint,<sup>2,3,13,14</sup> though squint is still present in the sidelobes and the nulls. Although they have the potential to be scanned rapidly, these systems are not adaptive and are able to process only linear or planar arrays and not ones that are conformal, irregular, or dynamically flexing. In addition, these fiber-based systems do not provide for a mechanism of adaptively weighting the array function to null out jammers or simultaneously point multiple beams. Moreover, fiber-optic TTD networks, even the elegant wavelength-tuned dispersive,<sup>15</sup> fiber prism,<sup>3</sup> or grating-reflective approaches,<sup>16</sup> can create extreme fiber management problems.

Our research group under K. Wagner previously developed adaptive phased-array processing systems, using photorefractive crystals as the adaptive weights that achieved 45 dB of narrow-band jammer nulling, and had the potential capability for TTD processing, but in a complex frequency-domain implementation.<sup>17</sup> A further drawback of our previous system was that to perform TTD beam forming directly on large arrays in the optical domain it was necessary to incorporate as large an optical TDL with as large an optical path length as the size of the phased array—yet over this propagation distance the short optical wavelength makes diffractive spreading a significant problem unless reimaging (as in a stable Herriot cell resonator) or fiber waveguiding is used. Our previous system used wedged or tilted Fabry–Perot etalons to incorporate this delay, which was manifested as arrays of frequency-selective bandpass filters with a resolution inverse to the required delay; however, achieving such resolution on parallel arrays of signals presented a significant engineering challenge. The photonic implementation of the BEAMTAP network presented here is a substantial simplification and outgrowth of this previous research and represents an attractive alternative to the limitations of previous optical approaches.<sup>18</sup> The key is the use of a single traveling-wave detector such as a 1-D time-delay-and-integrate charge-coupled de-

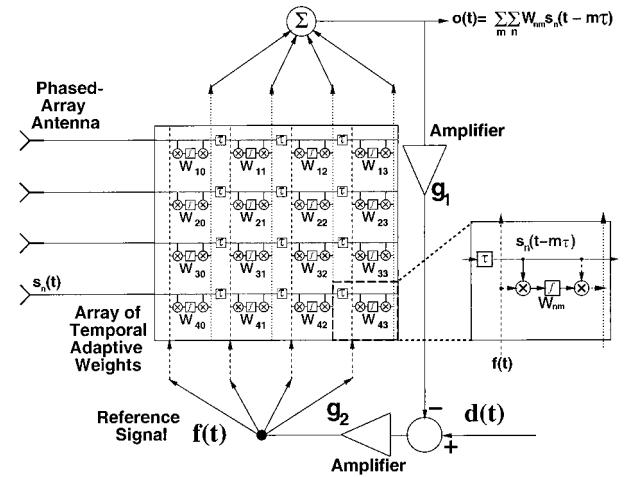


Fig. 2. Conventional time-delay-and-sum approach to adaptive array processing for broadband squint-free TTD beam forming with LMS adaptation based on a desired signal and a correlation-cancellation-loop feedback, where the desired signal  $d(t)$  is subtracted from the output signal  $o(t)$  to produce the feedback signal  $f(t)$ . Each weight is formed by integration of the multiplication of the feedback with the delayed antenna signals. The delayed antenna signals are then multiplied by the weights and summed to produce the output.

vice (TDI CCD)<sup>19,20</sup> or a photoconductive traveling-fringes detector (TFD)<sup>21,22</sup> to allow for the generation of the necessary tap-in time delays in the electrical (rather than the optical) domain, whereas the tap-out delay line can be implemented compactly with acoustic delay lines such as AO Bragg cells for the input. However, all the adaptive timing, phasing, and weighting is still done in the optical domain.

### A. Conventional Time-Delay-and-Sum Adaptive Beam Former

In conventional time-domain beam forming, as shown schematically in Fig. 1 and with the details of the least-mean-square (LMS) algorithm in Fig. 2, each of the  $N$  antenna outputs  $s_n(t)$  (for  $n = 1, \dots, N$ ) is input to a TDL, which is represented for discrete delays as  $s_n(t - m\tau)$  (for  $m = 0, \dots, M - 1$ ), where the temporal spacing between taps is  $\tau$  and the total delay of the TDL is  $T \equiv (M - 1)\tau = M'\tau$  where  $M'$  is the total number of time delays and is represented in continuous notation as  $s_n(t - t')$  for  $0 < t' < T$ . The output consists of a sum of each antenna output causally convolved with finite impulse responses  $W_{nm}^*$  of duration  $T$ ,

$$o(t) = \sum_{n=1}^N \sum_{m=0}^{M-1} s_n(t - m\tau) W_{nm}^*. \quad (1)$$

The weighted impulse response filter  $W_{nm}^*$  of each antenna element is usually calculated by an adaptive algorithm, and for the common LMS style of algorithms<sup>23,24</sup> the weights are calculated as a correlation coefficient between each delayed antenna signal and a signal  $f(t)$ —which is either derived from a feedback loop or is an *a priori* known reference signal. The most common form of error-driven feedback is when

$f(t) = d(t) - o(t)$  for some desired signal  $d(t)$ . Thus the weighted impulse response filter is given by

$$W_{nm}^* = \int_{-\infty}^t s_n^*(t_1 - m\tau) f(t_1) dt_1. \quad (2)$$

The time dependence of the weights that are due to adaptation up through time  $t$  is slow and can often be assumed constant over the duration of the convolution with the signals. Given this form of the adaptive weight matrix, the output can be written as

$$\begin{aligned} o(t) &= \sum_{n=1}^N \sum_{m=0}^{M-1} s_n(t - m\tau) W_{nm}^* \\ &= \sum_{n=1}^N \sum_{m=0}^{M-1} s_n(t - m\tau) \int_{-\infty}^t s_n^*(t_1 - m\tau) f(t_1) dt_1 \\ &= \sum_n \sum_m s_n(t - m\tau) \int_{-\infty}^t s_n^*(t_1 - m\tau) \\ &\quad \times [d(t_1) - o(t_1)] dt_1. \end{aligned} \quad (3)$$

Solving for the output  $o(t)$  can be accomplished with a frequency-domain approach that yields a power-nulling spatiotemporal filter. Below we show a nearly identical output for our new BEAMTAP beam former that requires only two TDL's in comparison with the  $N$  TDL's required by this LMS time-delay-and-sum conventional approach.

### B. BEAMTAP Algorithm

In the new BEAMTAP algorithm shown in Fig. 3, each antenna element output  $s_n(t)$  is multiplied at every resolvable instant of time  $t$  by a linear array of weights  $W_{nm}^*$ , which are located along the corresponding row of the weight matrix. Each product is summed along the columns with the corresponding products from the other rows produced by the other array elements, and the resulting sum is input to a tap-in scrolling delay line, whose inputs at the  $m$ th tap-in position are given by a weighted sum over undelayed signals

$$Y_m(t) = \sum_{n=1}^N s_n(t) W_{nm}^*. \quad (4)$$

As the tap-in delay line spatially scrolls in time by increments of  $\tau$ , it accumulates the appropriate contributions from each column sum position, and after a particular moving sum traverses the entire delay-line aperture, the resulting output is the desired multiply weighted and delayed sum from the array,

$$o(t) = \sum_{m=0}^{M-1} Y_m(t - m\tau) = \sum_{m=0}^{M-1} \sum_{n=1}^N s_n(t - m\tau) W_{nm}^*. \quad (5)$$

Thus from any antenna element there is a path into the delay line at a position such that the output has

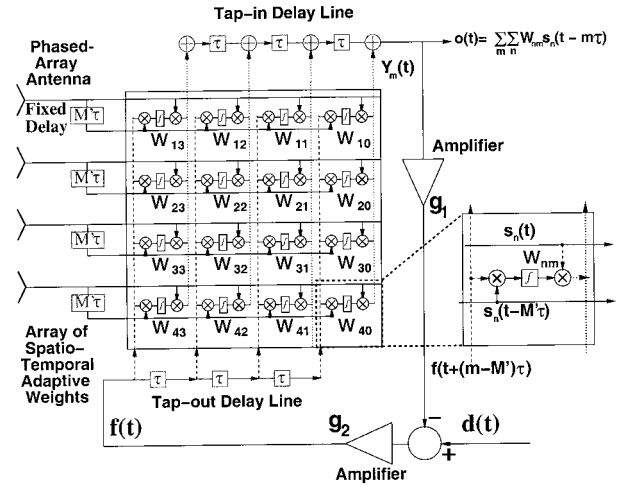


Fig. 3. BEAMTAP algorithm for broadband squint-free TTD beam forming with a single output tap-in delay line. For adaptive calculation of the weights within the array, the additional input TDL is also required. The desired signal  $d(t)$  is again subtracted from the output signal  $o(t)$  to produce the feedback signal  $f(t)$ . Here the variably delayed feedback is multiplied by the antenna signals delayed by  $T$  and integrated to produce the weights. The weights are then multiplied by the undelayed antenna signals, column summed, and input into the tap-in delay line.

the appropriate delay, and this is exactly equivalent to the conventional time-domain beam former given in Eq. (1). In a sense we have simply commuted the linear operation of multiple TDL's that have one weighted output from each tap position into a single multiple-input-delay line that addresses the same array of weights.

To operate as an adaptive phased array, the weights must be calculated in response to changes of the signal environment. The LMS algorithm can be readily implemented within the hardware-efficient BEAMTAP beamformer by inclusion of an input delay line and a correlator-integrator to calculate each adaptive weight in the  $M \times N$  array of weights. Each processing element in the weight matrix array contains an analog multiplier that multiplies the output of the tap-out delay line at that column with the sample from the phased array at that row. These products are locally time integrated to produce the adaptive weights as the appropriate correlation coefficients

$$W_{nm}^*(t) = \int_{-\infty}^t s_n^*(t_1) f\{t_1 + [m - (M - 1)]\tau\} dt_1. \quad (6)$$

In this expression  $m$  varies from 0 to  $M - 1$  so that the argument of  $f$  at the  $t$  limit of integration varies from  $t - (M - 1)\tau$  to  $t$  and is therefore always causal. These weights are then used as the coefficients in the subsequent array of multipliers to produce the appropriate beam-steered array output as the scrolling

sum of the adaptively weighted and column-summed contributions:

$$\begin{aligned}
o(t) &= \sum_m Y_m(t - m\tau) \\
&= \sum_m \sum_n \int_{-\infty}^t \delta[t' - (t - m\tau)] s_n(t') W_{nm}^*(t') dt' \\
&= \sum_{n,m} s_n(t - m\tau) \int_{-\infty}^{t-m\tau} s_n^*(t_1) f[t_1 + (m - M')\tau] dt_1 \\
&= \sum_{n,m} s_n(t - m\tau) \int_{-\infty}^t s_n^*(t_2 - m\tau) f(t_2 - M'\tau) dt_2.
\end{aligned} \tag{7}$$

Note that this adaptive algorithm is the exact equivalent of the time-domain LMS adaptive beam former shown in Eq. (3), except for the simple time shift of the correlation signal  $f(t)$  by  $M'\tau = (M - 1)\tau$ . For correlating against a known reference signal  $f(t)$  as required in main-beam formation,<sup>25,26</sup> this time delay is readily accommodated by advancing the reference appropriately. This unwanted delay is more troublesome in correlation-cancellation-loop algorithms as required for jammer nulling, in which the feedback signal is given by the desired reference minus the output  $f(t) = d(t) - o(t)$ , since the output cannot be advanced in time [this would require us to know  $o(t)$  before it has been generated]. However, we can solve this dilemma by delaying the antenna signals,  $s_n(t)$ , which are used to write the weights relative to the signals used for reading the weights, by an additional  $T = M'\tau$ :

$$\begin{aligned}
o(t) &= \sum_n \sum_m s_n(t - m\tau) \int_{-\infty}^t s_n^*(t_2 - m\tau - M'\tau) \\
&\quad \times f(t_2 - M'\tau) dt_2 \\
&= \sum_n \sum_m s_n(t - m\tau) \int_{-\infty}^{t-M'\tau} s_n^*(t_2 - m\tau) \\
&\quad \times [d(t_2) - o(t_2)] dt_2.
\end{aligned} \tag{8}$$

This produces the correct relative delay between  $s_n(t)$  and  $o(t)$  inside the weight integral, and  $d(t)$  can be delayed as desired. The only difference from Eq. (3) is the upper limit of the integral. This means that the weights are being updated and adapted by the delayed product of  $s_n(t)$  and  $f(t)$ , which will be inconsequential for realistic slow adaptation rates or at steady-state operation. It should also be noted that although this approach does require a second version of each antenna signal,  $s_n(t)$ , delayed by a fixed amount,  $M'\tau$ , it does not require a TDL version of these signals.

A note on the convergence properties of this algorithm are in order, since conventional LMS array processing with digital signal-processing techniques are known to converge only for a limited feedback gain.<sup>27,28</sup> The real-time array adaptation in

BEAMTAP is a continuous-time adaptive algorithm, since the weights evolve continuously even though the output waveform may be sampled by the quantized charge packets of an output discrete shift register (the tap-in delay line) in addition to having the array dimension always being sampled. However, since the adaptive weights are updated continuously and are governed by a first-order differential equation that is always guaranteed to converge, increasing the feedback gain will not lead to oscillations and unbounded weight growth as in sampled adaptation. Instead, it will simply increase the adaptation speed and increase the null depths.<sup>27</sup> It is important to note, though, that noise in the system and the unwanted feedthrough of the writing beam onto the velocity-matched traveling-detector array can lead to loop oscillation and will present a practical limit on the speed of adaptation.<sup>29</sup>

The BEAMTAP beam-forming algorithm is especially well suited to a photonic implementation of adaptive beam-forming and jammer-nulling signal processing in very large phased arrays. The optical approach allows for an enormous number of adaptive weights ( $10^9$ ) to be stored in the volume of a photorefractive crystal, thereby enabling the broadband processing of very large arrays as the analog multiplication, integration, and final multiplication needed to write and read out the weight matrix are accomplished through the interference, grating formation, and subsequent diffraction, respectively, of light within the crystal itself. Furthermore, the corresponding digital processing load that would be required for solving these large, broadband, adaptive-array signal-processing problems for a 1-GHz bandwidth broadband array with 1000 elements and 1000 taps/element exceeds  $10^{15}$  multiply accumulate operations/s just for the weight readout. The adaptation with LMS is at least as computationally intensive, and covariance matrix estimation and inversion techniques typically used in digital adaptive-array processing are prohibitive for this case, in which the covariance matrix is  $10^6 \times 10^6$  elements. Such a matrix would require  $O(N^3) = 10^{18}$  operations to initially invert, and then would require  $O(N^2) = 10^{12}$  operations to perturb the matrix inverse and weights at each adaptation interval, desired to be as fast as microseconds, yielding  $10^{18}$  operations/s throughput requirements. To decrease this insurmountable digital computational load, restrictive assumptions are often made on the number of signals and jammers, allowing for efficient subspace adaptation algorithms to be used, which perform acceptably until the number of signals becomes too large. Another approach is to employ subarray techniques that yield smaller numbers of digitized signals (and corresponding adaptive degrees of freedom), reducing the digital computational load for simpler signal environments. Thus restrictive assumptions on the number of signals are often made to decrease the digital computation load (allowing for more efficient subspace adaptivity); or alternatively, subarray tech-

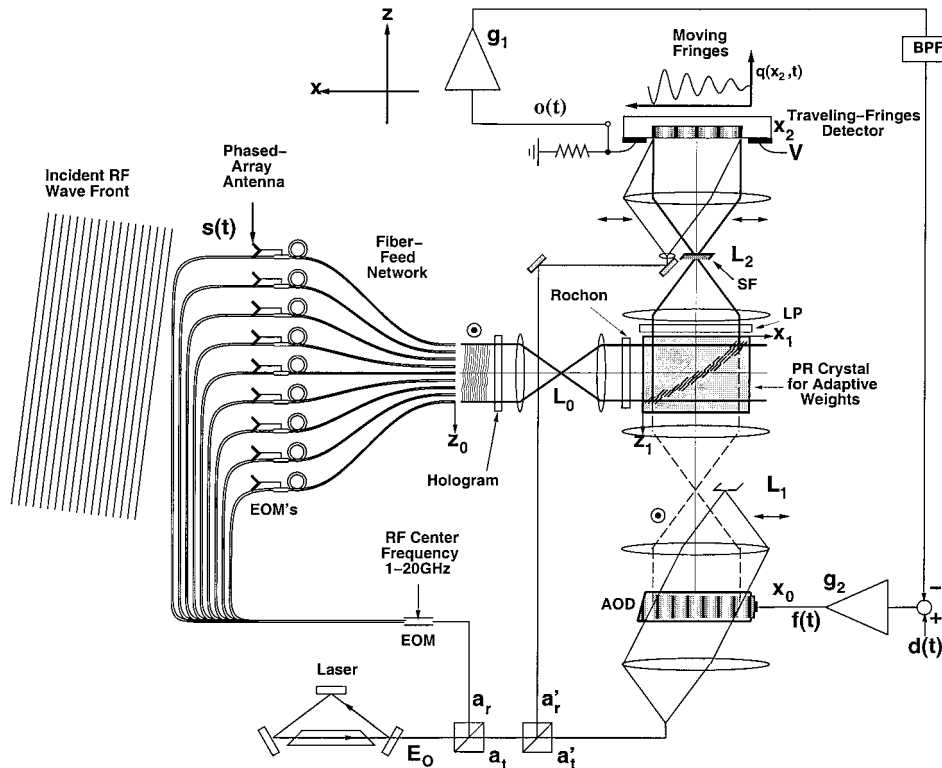


Fig. 4. Optical architecture of BEAMTAP. A single coherent laser is divided with two beam splitters with amplitude reflectances  $a_r$  and  $a'_r$ , and amplitude transmittances  $a_t$  and  $a'_t$ , respectively, to drive both the fiber-feed network and the BEAMTAP processor—the fiber-feed network from the phased array is shown on the left-hand side. The diffracted light from the AOD interferes with signals from the array, which are imaged through lens system  $L_0$  to form gratings in the photorefractive crystal (PR crystal). Diffraction of the phased-array signals off this grating is detected by a synchronous TFD, which has a carrier velocity matched to the magnified acoustic velocity of the AOD by the lens systems  $L_1$  and  $L_2$ —producing a resonant charge carrier distribution  $q(x_2, t)$ . The output signal  $o(t)$  is amplified by  $g_1$ , passed through a bandpass filter (BPF), subtracted from the desired signal  $d(t)$ , amplified by  $g_2$ , and fed back into the AOD as the feedback signal  $f(t)$  to close the adaptive feedback loop necessary for the system to cancel any jamming signals present in the signal environment. A Rochon prism, linear polarizer (LP), and spatial filter (SF) are used for the read–write isolation of the AOD beam from the diffracted phased-array signals off the grating. The illustrated system places the photorefractive crystal in the image plane of the fiber feed and the AOD, and uses orthogonally propagating fields, for illustrative purposes.

niques with smaller numbers of adaptive degrees of freedom are used so that acceptable performance can be obtained until the number of signals becomes too large. Unless the problem is simplified, these digital computation loads exceed even the most optimistic performance projections for massively parallel, wafer-scale, and multi-chip-module digital signal-processing implementations, making this an appropriate problem for an optical signal-processing solution. In addition, rf photonic techniques allow for wide instantaneous bandwidths of 1–2 GHz, limited only by AO technology, which can be tuned over the full 1–20-GHz rf band with only a single additional electro-optic modulator (EOM) with no mixers or downconverters. Fully photonic processing with only one traveling-wave detector avoids noise contributions from the  $N$  detectors often required in parallel photonic link systems, thereby potentially improving system dynamic range. Therefore the rf photonic techniques presented here appear to be the only viable solution for these next-generation fully adaptive, large, wideband array processing systems.

### 3. Optical System Analysis

In this section, we perform a detailed analysis of the BEAMTAP optical system. The analysis includes many of the necessary complexities of double-sideband amplitude modulation in EO devices, single-sideband polarization-switching diffraction in the AOD, finite response time of the photorefractive crystals, read–write multiplexing and isolation with polarization and angle multiplexing, as well as spatial filtering of the diffracted orders, interferometric detection on the traveling fringes detector (TFD), and the time delays of the feedback loop. This analysis not only validates the idealized algorithmic analysis presented in Subsection 2.B but also provides valuable information on the necessity of proper alignment of the interferometric beams, the unavoidable bias buildup if a TDI CCD is used for the tap-in delay line, the difficulty with low modulation depths of the EO devices, and the processor bandwidth limitation due to feedback delay<sup>30</sup> and its mitigation with the compensating delay of the writing beams. However, the analysis does neglect diffraction, laser drift, and noise (relative intensity,

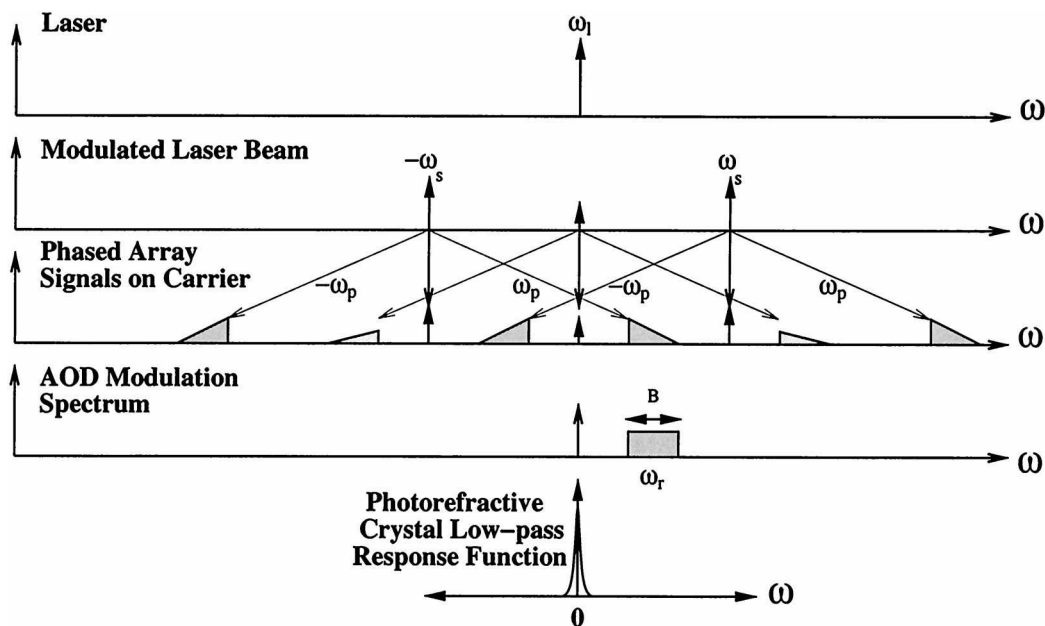


Fig. 5. Frequency offset scheme for the phased-array radar processor that allows for tuning of the processing bandwidth  $B$  (determined by the AOD bandwidth and typically limited to 1–2 GHz) anywhere within the rf spectrum spanned by the EOM's bandwidths. The laser beam  $\omega_l$  is premodulated by  $\pm\omega_s$  (in this case only the negative sideband is used), and then the rf signals modulate within a bandwidth of  $B$  and are offset by  $\pm\omega_p$ , such that the desired mix term overlaps the bandwidth  $B$  and carrier  $\omega_r$  of the AOD. The photorefractive crystal responds only to the near-dc interferometric products between the phased-array signals and AO diffractions, and all moving gratings wash out.

shot, thermal, etc.) for the sake of simplicity. Numerical simulations of the operation of the processor are then presented that demonstrate several of the compensation mechanisms that are intrinsic to the adaptive holographic weight matrix.

#### A. System Overview

Figure 4 shows one possible optical architecture for the implementation of the BEAMTAP system with the photorefractive crystal in the image plane of the AOD. (Alternative systems could use the photorefractive crystal in a Fourier or Fresnel plane of either arm; the undiffracted beam from the AOD could be used as a reference; or an alternative read–write multiplexing scheme could be used<sup>29</sup>—the key requirement is that the AOD be imaged and velocity matched onto the TFD.) In the illustrated system a single powerful low-noise laser is divided by a beam splitter (amplitude reflectance  $a_r$ ) and frequency shifted by an EOM to within 1 GHz of the rf center frequency (typically in the range of 1–20 GHz). This frequency-shifted beam is then distributed through a fiber-feed network and is modulated by EOM's with the signals  $s_n(t)$  coming from each of the elements of the phased-array antenna. The first frequency-shifting EOM in combination with the antenna EOM's in the phased-array, operating at the rf center frequency, produce a frequency shift commensurate with that produced by the AOD, allowing for processing of rf signals anywhere within the full 1–20-GHz rf band. The rf frequency domain for double-sideband modulation is illustrated in Fig. 5, although only one sideband is used in the analysis. Each of the rf-modulated signals is then transmitted from the mod-

ulators in the phased array through the fiber-feed network to an array of terminated fibers. These fibers can be in any topological arrangement (1-D linear array, 2-D hexagonal array, random, etc.) and with an arbitrary permutation with respect to the spatial topology of the phased array, but for simplicity, in this analysis we assume that there is a 1-to-1 mapping between an equispaced linear phased-array antenna and an equispaced array of optical fibers. The modulated signals from the fiber-feed network are then imaged into the photorefractive crystal by use of the  $4f$  system  $L_0$ .

The transmitted beam from the first beam splitter (amplitude transmittance  $a_t = \sqrt{1 - a_r^2}$ ) is split into an interferometric reference beam (amplitude  $a_t a_r' E_o$ ) and an input to the AO Bragg cell (amplitude  $a_t a_t' E_o$ ). The beam is expanded, collimated, and tilted to the Bragg angle, whereby a feedback signal  $f(t)$  applied to the AOD launches a propagating acoustic wave that modulates the incoming light by means of the AO effect and diffracts it at the Bragg angle. Tangential matching in an anisotropic polarization switching device is used here so that the diffracted beam has an orthogonal polarization to that of the undiffracted beam. The diffracted beam is then imaged into the photorefractive crystal by use of the  $4f$  lens system  $L_1$ , whereas the undiffracted beam is blocked in the Fourier plane of the lens system  $L_1$  by use of a spatial filter. The diffracted beam from the AOD interferes with the spatiotemporally modulated optical field launched by the fiber-feed network, and the time integration of this interference pattern produces  $45^\circ$  gratings at positions corresponding to delays where the beam containing the desired signal

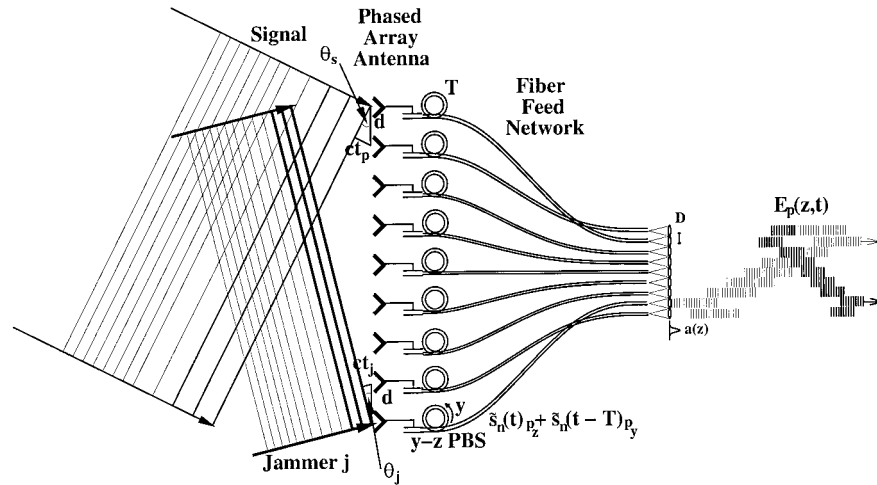


Fig. 6. Example of a linear equispaced phased array and a random fiber-optic feed network. A broadband rf signal is incident from one angle and a jammer  $j$  from another angle onto a phased-array antenna with element spacing  $d$ , creating time delays  $t_p$  and  $t_j$  between the elements of the array for the signal and jammer, respectively. Both signals are modulated onto a much-higher-frequency optical carrier and transduced into the optical domain; then these signals are propagated through an optical fiber-feed manifold to a linear array of polished fiber ends. While propagating through the polarization-maintaining fiber, each beam passes through a polarizing beam splitter (PBS) so that the  $\hat{p}_y$ -polarized writing beam passes through the delay loop and experiences a time delay  $T$  with respect to the  $\hat{p}_z$ -polarized reading beam. Typical fiber cores of  $8\ \mu\text{m}$  and spacings of  $250\ \mu\text{m}$  are shown being collimated by a lenslet array, which allows us to make the simplifying assumption of propagation without diffraction used in the analysis of this section. These lenslets are not required in the real system, and the simplifying assumption of propagation without diffraction is not required in practice, but is illustrated here for analytic and diagrammatic simplicity.

$d(t)$  is well correlated with one of the beams from the fibers containing the signals from the antenna array  $s_n(t)$ .

Light from the fiber-feed network then diffracts off the gratings in the crystal. The time delays (both due to the inherent delays produced by the phased-array antenna and to random time delays introduced by the small length mismatches between the fibers) are transformed into diffracted beams at spatial positions proportional to their respective time delays. These position-dependent time delays will be delayed and summed with appropriate time alignment by detection with a time-integrating traveling-wave detector array matched to the velocity of the image of the AOD. Read-write multiplexing with angle and polarization encoding is implemented by use of a quarter-wave plate, Rochon prism, polarizer, and spatial filter to isolate the diffracted readout beam of the phased array from the diffracted write beam of the AOD. Details of read-write multiplexing architectures have been covered in previous publications,<sup>17,31</sup> so are delineated only briefly in this paper.

The diffracted signals are then imaged onto a time-integrating traveling-wave detector implemented with a TFD<sup>21,22</sup> where they interfere with the reference beam from the laser—which must be at the exact angle that the undiffracted dc beam from the AOD would have occupied if it had not been blocked. At each resolvable temporal increment, the TFD is read out after the corresponding charge packet has traversed the length of the detector, accumulating and delaying detected signal contributions from each location. The resulting output waveform is an adap-

tively weighted and coherently reconstructed version of the signal.<sup>18</sup> For closed-loop adaptive processing, this output signal  $o(t)$  is then subtracted from our desired signal  $d(t)$ , which is well correlated with the signal of interest  $s(t)$  (for instance, a known chirp can be broadcast along with an unknown pseudorandom noise waveform). This difference signal generates the feedback signal  $f(t) = d(t) - o(t)$ , which is then fed back into the AOD. The feedback loop provides the necessary error-driven adaptation required for beam steering the main beam toward the desired signal source and nulling out any undesired jammers present in the signal environment at the input of the phased-array antenna—which can include both near-field and far-field, as well as narrow-band and broadband, jammers.

## B. Acousto-Optic Device

The single-sideband feedback signal amplified and applied to the AOD transducer consists of the difference between the processor output signal  $o(t)$  and the steering rf signal  $d(t)$  such that  $\tilde{f}(t) = g_2[\tilde{d}(t - t_d) - g_1\tilde{o}(t - t_f)]$  (where  $g_1$  and  $g_2$  are the gains of the photodetector output and the AOD power amplifier, respectively;  $t_d$  is a constant reference delay that accounts for the arbitrary timing of the desired signal to ensure that the correlation peak with the arriving array signals is within the AOD aperture; and  $t_f$  is the feedback delay due to propagation through wires, amplifiers, and the bandpass filter). The signal is octave-bandwidth, limited around a rf center frequency  $\omega_r$ , which is implicitly included in the analytic signal representation  $f_0(t)$ ,  $\tilde{f}(t) = f_0(t)\exp(-i\omega_r t)$ ,

where  $f_o(t)$  is a real bandlimited baseband signal. The signal will propagate through the AOD at the acoustic velocity  $v_A$  in the positive  $x$  direction at a plane  $x_0$  and time  $t_0$ , resulting in a modulated output

$$\begin{aligned} \tilde{f}(x_0, t_0) &= g_2 \left[ \tilde{d} \left( t_0 - t_d - \frac{x_0}{v_A} - t_{r_1} \right) \right. \\ &\quad \left. - g_1 \tilde{o} \left( t_0 - t_f - \frac{x_0}{v_A} - t_{r_1} \right) \right] \\ &\equiv \tilde{f} \left( t_0 - \frac{x_0}{v_A} - t_{r_1} \right), \end{aligned} \quad (9)$$

where  $t_{r_1}$  allows for the AOD aperture to be centered in the optical system.

A collimated optical beam with an angular carrier frequency  $\omega_l$ , which is incident on the AOD at the Bragg angle  $\theta_B = \sin^{-1} |\mathbf{k}_B|/|\mathbf{k}_0|$ , where  $|\mathbf{k}_0| = \omega_l/c = 2\pi/\lambda_0$  is the free-space wave number and  $|\mathbf{k}_B| = \omega_A/c$  is the acoustic wave number, will diffract off the acoustic wave to produce a diffracted beam and an undiffracted beam

$$\begin{aligned} E_A(x_0, t_0) &= a_t a'_t E_o \exp[i(k_B x_0 - \omega_l t_0)] \\ &\quad \times \left[ (1 - \eta_{\text{AO}}^2 |\tilde{f}|^2)^{1/2} \hat{p}_x \right. \\ &\quad \left. + \eta_{\text{AO}} \tilde{f} \left( t_0 - \frac{x_0}{v_A} - t_{r_1} \right) \hat{p}_y \right], \end{aligned} \quad (10)$$

where  $a_t = \sqrt{1 - a_r^2}$  is the amplitude transmittance of the light from the beam splitter,  $\eta_{\text{AO}}$  is the amplitude diffraction efficiency of the AOD per volt, and  $|\tilde{f}(t_0 - x_0/v_A - t_{r_1})|^2$  has been written as  $|\tilde{f}|^2$  in the undiffracted beam. Anisotropic diffraction in the AOD results in diffracted and undiffracted beams with orthogonal polarizations,  $\hat{p}_y$  and  $\hat{p}_x$ , respectively. The undiffracted beam can be used as an interferometric reference that is automatically aligned at the correct angle to produce a nondispersive traveling-fringe pattern on the tap-out detector. The drawback to this design is that this strong unmodulated beam will cause erasure and decrease modulation depth in the photorefractive crystal, resulting in reduced diffraction efficiency from the weight matrix. In addition, the undiffracted beam from the AOD may have too much residual modulation because of its nonlinear dependence on the signal's strength being injected into the tap-in device. A clean reference beam can be split off before the AOD and routed to avoid passing through the crystal before being reinjected onto the TFD at the correct angle so that it interferes with the diffracted signal beam to produce a nondispersive traveling-fringe pattern, as shown in Fig. 4.

The diffracted and the undiffracted beams are Fourier transformed by the first lens so that the undiffracted beam can be blocked. The diffracted beam is then inverse transformed by the second lens to produce an image of the AOD in the crystal. Noting that  $m_1 = x_1/x_0$  is the magnification of lens system  $L_1$ , the electric field distribution can be approximated

within the photorefractive crystal. For the sake of simplicity, the effects that are due to diffraction of the propagating fields are neglected in this analysis. Instead, we account for propagation with a phase accumulation so that the field within the photorefractive crystal is

$$\begin{aligned} E_A(x, z, t_0) &= a_t a'_t E_o \exp[i(k_B x - \omega_l t_0)] \\ &\quad \times \eta_{\text{AO}} \tilde{f} \left( t_0 - \frac{x}{v} - t_{r_1} \right) \exp(ikz) \hat{p}_y, \end{aligned} \quad (11)$$

where  $k = 2\pi n/\lambda_0$  is the wave-vector length in the photorefractive crystal of index  $n$  and the velocity  $v_a$  has been scaled by the magnification to a velocity  $v$ . A detailed analysis demonstrating that the effects due to diffraction are holographically compensated for by the processor has already been presented.<sup>32</sup>

### C. Phased Array

Next, consider the fiber-optic modulation topology shown in Fig. 6. A desired signal produced by a broadband far-field plane wave arriving on a linear equally spaced array at some angle  $\theta_s$  is illustrated. The signal at a particular element  $n$  will have a differential time delay between adjacent phased-array elements  $t_p = d/c \sin \theta_s$ , where  $d$  is the spacing between the elements and  $c$  is the speed of light. The desired signal at the  $n$ th element of an equispaced array can thus be described as  $\tilde{s}_n^d = \tilde{r}(t - nt_p)$ . Any far-field jammers present within the signal environment will also experience incremental time delays given by  $t_j = d/c \sin \theta_j$ . If more than one jammer is present, the jamming signal at the  $n$ th element can be described as  $\tilde{s}_n^j = \sum_j \tilde{j}_j(t - nt_j)$ . We will assume that the desired signal and any jamming signals are in a frequency band no greater than the bandwidth of the AOD centered around  $\omega_p$ , but that this center frequency can be anywhere within the modulation bandwidth of the EOM's. A single sideband of the signal detected by the  $n$ th array element is thus

$$\tilde{s}_n(t) = \tilde{r}(t - nt_p) + \sum_j \tilde{j}_j(t - nt_j), \quad (12)$$

where the carrier term  $\omega_p$  is implicit within the single-sideband analytic representations  $\tilde{r}(t)$  and  $\tilde{j}(t)$ . More generally, the  $nt_p$  and/or the  $nt_j$  term can instead be an arbitrary function of  $n$  to represent any random time delays caused by positional errors in the placement of the array elements, conformal arrays, near-field signals or jammers, or an arbitrary spatial permutation of the topology of the array of fibers with respect to the array elements.

Amplitude modulation by the first frequency shift-ing EOM before the phased-array offsets the light carrier  $\omega_l$  by  $\pm\omega_s$  giving a new carrier  $\omega_c = \omega_l \pm \omega_s$  (where we will choose to use only one of the sidebands and reject the other with a fiber bandpass filter). After it is amplitude modulated by the array of  $N$  EOM antenna transducers in the fiber-feed network,

the electric field distribution launched into the processor by the fibers is

$$E_P(z_0, t_0) = \frac{a_r}{\sqrt{N}} E_0 \sum_{n=1}^N \exp\{-i[\omega_c(t_0 - t_n)]\} a(z_0 - nD_0) \times [\sqrt{1 - \eta_p^2 |\tilde{s}_n|^2} + \eta_p \tilde{s}_n(t_0 - t_n - T) + \eta_p^* \tilde{s}_n^*(t_0 - t_n - T)] \hat{p}_y, \quad (13)$$

where  $|\tilde{s}_n|^2 = |\tilde{r}(t_0 - nt_p - t_n - T) + \sum_j \tilde{j}_j(t_0 - nt_j - t_n - T)|^2$ . In Eq. (13),  $a_r/\sqrt{N}$  is the amplitude of the light after equal splitting into each of the  $N$  fibers.  $a(z_0 - nD_0)$  is the aperture function (typically a Gaussian distribution with a width of 5–9  $\mu\text{m}$ ) of the  $n$ th fiber, located at position  $nD_0$  where  $D_0$  is the spacing between the fibers. For fibers in a silicon  $V$ -groove array, a typical value of  $D_0$  might be 250  $\mu\text{m}$ .  $\eta_p$  is the amplitude-modulation efficiency of the EOM's per volt and is assumed to be the same for all modulators.  $t_n$  is a random time delay that accounts for phase and time shifts due to fiber length mismatches, which can change with temperature variations and shifting antenna configurations. These mismatches affect both the optical carrier  $\omega_c$  (for submicrometer mismatches) and the microwave carrier  $\omega_r$  (for centimeter mismatches) and must be accounted for in the formalism.  $T$  is the round-trip feedback loop time delay, which, as described in Subsection 2.B, is necessary to ensure causality of the final output signal  $o(t)$ . This time delay is implemented on each phased-array signal by use of a polarizing beam splitter in each fiber, which causes the  $\hat{p}_y$ -polarized writing beam to pass through a fiber-delay loop while the  $\hat{p}_z$  polarized reading beam propagates directly through the fiber-feed network. Polarization-preserving fiber is used to ensure that the polarizations of these two beams are maintained while propagating through the fiber so that the output writing beam will have the same polarization as the diffracted beam from the AOD  $\hat{p}_y$ . Thus Eq. (13) describes the electric field distribution of the writing beam while the reading beam will be  $\hat{p}_z$  polarized without the delay  $T$ .

It is vital to realize that these lengths can easily be perturbed by small motions of the fibers or by temperature changes (thereby giving rise to  $t_n$ ), and although such fluctuations will have no effect on the rf carrier phase, the optical phase can swing wildly and must be compensated through adaptation. In the system presented in this paper, adaptation will occur in a time well below 1 ms (much faster than the photorefractive hologram response time<sup>17</sup>), which should be sufficient to compensate for these phase fluctuations. We are representing the EOM as being operated as an amplitude modulator, but for the sake of simplicity the complex conjugate term will be subsequently dropped to produce a single-sideband phase modulator. Ideally, we would use single-sideband suppressed carrier modulators, which would eliminate the dc term as well. Including these terms in the analysis yields essentially the same overall result, since they are at the wrong frequency to record stationary gratings and thus will

not affect the photorefractive crystal except through incoherent erasure. However, in addition to the previously noted considerations, the phase in the  $\hat{p}_y$ -polarized fiber-delay loops must be stabilized with respect to the undelayed  $\hat{p}_z$ -polarized phases for a given fiber. Although this can be accomplished with individual polarization-locking feedback-to-loop fiber stretchers, a single novelty filter<sup>33</sup> can be used instead to stabilize all of the fiber loops simultaneously (and to remove the unwanted dc term as well). We leave the details of this loop stabilization to a subsequent paper and henceforth assume a phase-stable delay by  $T$  in all of the fiber loops.

This phased-array signal beam is then imaged through lens system  $L_0$ , and noting that  $m_0 = z_1/z_0 = D_1/D_0$ , the electric field distribution within the photorefractive crystal can be described when we include a propagation term that represents phase accumulation (in the negative  $x$  direction)

$$E_P(x, z, t_0) = \frac{a_r}{\sqrt{N}} E_0 \sum_{n=1}^N \exp\{-i[\omega_l(t_0 - t_n)]\} a(z - nD) \times [(1 - \eta_p^2 |\tilde{s}_n|^2)^{1/2} + \eta_p \tilde{s}_n(t_0 - t_n - T)] \times \exp(-ikx) \hat{p}_y, \quad (14)$$

where the offset frequency of  $\omega_s$  has now been incorporated implicitly into  $\tilde{s}_n(t_0)$ . We will choose the modulation frequencies such that  $\omega_r = \omega_s + \omega_p$ , so the resulting modulation produced by the EOM's overlaps with the Doppler frequencies produced by the AOD, as shown previously in Fig. 5.

#### D. Grating Formation

As the optical beam from the AOD interacts with the beam from the phased array, and if the frequency spectra of the two beams overlap, an index grating is formed within the photorefractive crystal, owing to the stationary interference pattern. With first-order analysis, the grating evolution can be approximated by

$$G(x, z, t') = \beta \int_{-\infty}^{t'} E_A(x, z, t_0) E_P^*(x, z, t_0) \times \exp\left[-\frac{(t' - t_0)}{\tau}\right] dt_0 + \text{c.c.}, \quad (15)$$

where  $\beta$  is the sensitivity of the crystal ( $\text{cm}^2/\text{J}$ ),  $\tau$  is the photorefractive time constant, and the details of the photorefractive dynamics have been idealized from their much more complex form.<sup>34</sup> For times  $t' \gg \tau$  the convolution with  $\exp(-t_0/\tau)$  results in a causal Lorentzian low-pass filter in the temporal frequency domain with a width  $\Delta f = 1/(2\pi\tau)$ , typically in the range of hertz to kilohertz. Thus only stationary gratings can be written in the photorefractive crystal between equally Doppler-frequency-shifted beams, which are then weighted by the photorefractive time constant  $\tau$ , which in turn is inversely proportional to the dc intensity level  $\tau \propto \tau_0/I_{\text{dc}}$ , where  $I_{\text{dc}} = |E_A(x, z, t)|^2 + |E_P(x, z, t)|^2$ . The spatial-frequency response of the photorefractive crystal selects only high-



## Read-Write Multiplexing Technique

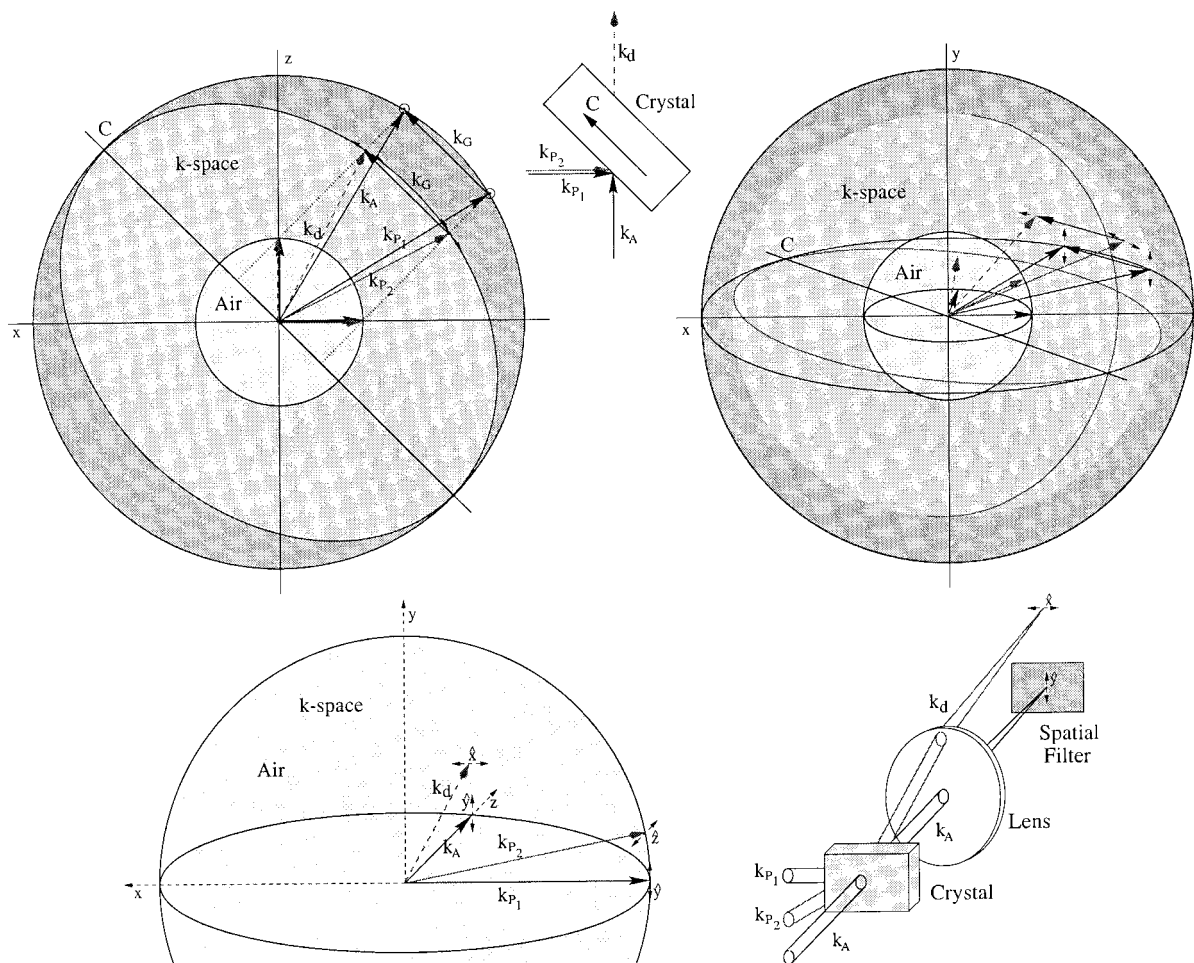


Fig. 7.  $k$ -space representation of the polarization, angle, and time-multiplexed recording and readout geometry in strontium barium niobate (SBN) used to separate the diffracted phased-array beam  $\mathbf{k}_d$  from the AOD beam  $\mathbf{k}_A$  used to write the grating. The upper left-hand portion of the figure is a 2-D projection of the three-dimensional momentum space on the right-hand side, where the three beams incident on the photorefractive (the write beam from the phased array  $\mathbf{k}_{P_1}$  with polarization  $\hat{p}_y$ , the vertically deflected read beam from the phased array  $\mathbf{k}_{P_2}\hat{p}_z$ , and the diffracted AOD beam  $\mathbf{k}_A\hat{p}_y$ ) refract into the crystal and are projected onto the ordinary and extraordinary momentum surfaces, based on their respective polarizations. The deflected read beam has been tilted vertically in the direction of Bragg degeneracy, allowing for efficient light diffraction off the grating  $\mathbf{k}_G$  produced by the interference between  $\mathbf{k}_{P_1}$  and  $\mathbf{k}_A$ . This produces a diffracted beam  $\mathbf{k}_d$  with polarization  $\hat{p}_x$  (once refracted back into air), which is vertically tilted from the reference signal beam from the AOD  $\mathbf{k}_A$  with polarization  $\hat{p}_y$ , as can be seen in the bottom portion of the figure. A lens, when in conjunction with a spatial filter, can then be used to block the beam from the AOD while allowing for the diffracted beam to pass through the system. A polarizer can also be used to increase the overall isolation between the two beams.

after diffraction off the grating cancels with the phase of the grating dependent on  $z$ . As a result, each of the components of light that diffracts off the grating from the fibers picks up the same overall phase  $\exp(ikL)$  and therefore adds coherently. Because the fiber profiles do not overlap, the undiffracting fields are spatially orthogonal to one another so that  $n = n'$  and the two sums collapse, which allows the random phase delays present in the carrier  $\exp(i\omega_l t_n)$  to be canceled with the holographically encoded phase  $\exp(-i\omega_l t_n)$ .

The signal strength received from the phased-array antennas will usually be small, and electrical preamplification may be required at each element of the antenna before optical modulation, but even with

amplification the modulation depth of the EOM is typically  $\ll 1\%$ . Thus there are two consequences of the dc term: erasure of the desired grating—thereby decreasing the grating strength (and therefore the null depth), and unwanted diffraction of the dc term from each fiber off of the correlation grating from that fiber—thereby producing unwanted bias when detected on the TFD. The dc term in  $E_p$  that diffracts off the grating (although with an incorrect phase front that is due to the fiber time delays) could potentially be much stronger than the modulated term, creating such a strong bias that it could swamp out the signal of interest. The actual diffraction efficiency of the unmodulated dc terms from the phased array off the grat-

ings will depend on the details of the time delays  $t_n$ , but because of coherent superposition of the diffractions off different parts of the gratings, the diffraction efficiency will tend to be zero for large array sizes. To avoid any unwanted diffraction of the strong dc terms, the EOM's should use a suppressed carrier modulation scheme<sup>36</sup> (or a photorefractive novelty filter could be used at the phased-array fiber-feed outputs to remove the dc carrier term, as mentioned previously<sup>33</sup>). We will thus assume that the dc term is not present in  $E_p$ . Finally, noting that  $\int_0^L |\alpha(z - nD)|^2 dz = 1$  is just the total normalized optical power present in the  $n$ th fiber,

$$E_d(x_1, t') = \exp[i(k_B x_1 - \omega_l t')] \exp(ikL) \\ \times E_o \kappa_1 \sum_{n=1}^N \tilde{s}_n(t' - t_n) \int_{-\infty}^{t'} \tilde{f}\left(t_0 - \frac{x_1}{v} - t_{r_1}\right) \\ \times \tilde{s}_n^*(t_0 - t_n - T) dt_0 \hat{p}_z, \quad (19)$$

where  $\kappa_1 = \kappa_o a_r \eta_p / \sqrt{N}$ . Equation (19) shows that the diffracted output from the photorefractive crystal convolves the cross correlation between the feedback signal and the detected signal with the signals from the phased-array antenna, with the detected signal used in the cross correlation being delayed by the round-trip delay time  $T$  to ensure causality. Note that the random phase factors that were originally present in the beam have been holographically compensated for and have been removed from the diffracted signals. Over a region defined by the transverse width of the grating envelope we will see a traveling-wave version of the signals from the various elements of the phased array propagating at a velocity  $v$  independent of the arrival angle of the signal.

#### F. Read-Write Isolation

As described so far, the readout diffracted beam from the phased array is not separable in angle from the modulated write beam from the AOD. For our adaptive phased-array processor, it is important to be able to separate these two beams so that the writing beam can be completely blocked from the detector plane. Otherwise, any leakage of the writing beam onto the TFD will limit the available loop gain and, therefore, the processor null depth.<sup>29</sup> This can be accomplished in many ways by use of polarization, timing, or angle multiplexing—although the isolation ratios required (well in excess of 60 dB) are not achievable with polarization multiplexing by itself. Here we consider a scheme that first vertically (i.e., orthogonal to the interaction plane of Bragg selectivity) deflects the undelayed portion of the light from the phased-array fiber feed by a Rochon prism (with a small deflection angle  $\theta_r$  of the order of  $1^\circ$ ). As discussed above, the  $x$ -propagating writing and reading beams from the array feed have orthogonal polarizations ( $\hat{p}_y$  and  $\hat{p}_z$ , respectively), because of the polarizing beam splitter used in the fiber-feed network to ensure that the writing beam propagates through the fiber loop and is delayed by  $T$  with respect to the reading beam. The polarizations of the undeflected beam  $\hat{p}_y$  and the

deflected beam  $\hat{p}_z$  from the Rochon prism are shown in the  $k$ -space diagram in Fig. 7 and are designated as  $\mathbf{k}_{p_1}$  and  $\mathbf{k}_{p_2}$  for the writing and the reading beams, respectively. The reading beam is tilted vertically in the direction of Bragg degeneracy, allowing for efficient diffraction off the original grating  $\mathbf{k}_G$ , which was written between the two  $\hat{p}_y$ -polarized beams  $\mathbf{k}_{p_1}$  and  $\mathbf{k}_A$ , the beams from the phased array and the AOD, respectively. This produces a diffracted beam  $\mathbf{k}_d$ , which is vertically tilted from the reference signal beam from the AOD  $\mathbf{k}_A$  so that in the Fourier plane of the first lens in lens system  $L_2$  (with focal length  $F_2$ ) they are spatially separated by  $y_r = \tan \theta_r F_2$ , and the beam  $\mathbf{k}_A$  that wrote the grating can be blocked with a spatial filter.<sup>17</sup> A linear polarizer with the transmission axis in the  $x$  direction is also used to block the writing beam from the AOD (which is polarized in the  $\hat{p}_y$  direction) to increase the overall isolation ratio between the reading and the writing beams. This scheme requires that an  $xz$ -polarized beam (within the crystal) be efficiently diffracted into an  $xz$ -polarized beam at a different angle, which is actually a convenient geometry for high-diffraction-efficiency readout using  $r_{33}$  in crystallographically cut strontium barium niobate (SBN) with the  $c$  axis at a  $45^\circ$  angle with respect to the  $x$  and the  $z$  axes, as shown in the figure. Alternatively, an  $xz$ -polarized beam could be diffracted into a  $zx$ -polarized beam by use of the conventional geometry for high-diffraction-efficiency readout using  $r_{42}$  in barium titanate ( $\text{BaTiO}_3$ ) (either crystallographic or  $45^\circ$  cuts<sup>35,37</sup>).

At this point, the off-axis interferometric reference beam (at the laser frequency  $\omega_l$ ) needs to be reinjected. Its position should correspond to the position in the Fourier plane (shifted vertically by  $y_r$ ), where the dc beam from the AOD would have been imaged to if it had not been blocked in the first Fourier plane in lens system  $L_1$ . This can be done by placement of a fiber carrying the reference beam with amplitude  $a_t a_r' E_o$  at the correct position in the Fourier plane or by use of the appropriate pick off mirrors, as shown in Fig. 4. A final lens can then be used to retransform the diffracted beam coming from the phased array in the photorefractive crystal, and the injected interferometric reference beam, onto the TFD.

#### G. Interferometric Traveling-Fringes Detector

Assuming a magnification of the  $4f$  system of  $m_2$  and a realignment of the system axis in the vertically tilted plane, the total field at the TFD is

$$E_d(x_2, t') = E_o \exp[i(k_B x_2 - \omega_l t')] \\ \times \left[ a_t a_r' + \eta_D \kappa_1 \sum_{n=1}^N \tilde{s}_n(t' - t_n) \right. \\ \left. \times \int_{-\infty}^{t'} \tilde{f}\left(t_0 - \frac{x_2}{v_D} - t_{r_1}\right) \tilde{s}_n^*(t_0 - t_n - T) dt_0 \right] \hat{p}_x, \quad (20)$$

where  $m_2 = x_2/x_1$ ,  $\eta_D$  is the overall amplitude transmission of the diffracted beams through the read-write multiplexing architecture,  $v_D$  is the velocity  $v$  scaled by the magnification  $m_2$  so that it matches the detector velocity, and we have dropped the constant phase term  $\exp(ikL)$  without any loss of generality.

The intensity at the detector is given by

$$I(x_2, t') = (a_t a_r' E_0)^2 + (\eta_D \kappa_1)^2 \left| \sum_{n=1}^N \tilde{s}_n(t' - t_n) \times \int_{-\infty}^{t'} \tilde{f} \left( t_0 - \frac{x_2}{v_D} - t_{r_1} \right) \tilde{s}_n^*(t_0 - t_n - T) dt_0 \right|^2 + \kappa_2 \sum_{n=1}^N \tilde{s}_n(t' - t_n) \int_{-\infty}^{t'} \tilde{f} \left( t_0 - \frac{x_2}{v_D} - t_{r_1} \right) \times \tilde{s}_n^*(t_0 - t_n - T) dt_0 + \text{c.c.}, \quad (21)$$

where  $\kappa_2 = a_t a_r' \eta_D \kappa_1$ .

The TFD is based on the synchronous drift of photogenerated carriers with a moving interference pattern<sup>21,22</sup> generated by interfering two beams of light at different frequencies—the diffracted beam from the phased array and the interferometric reference beam, and the device is also used to time delay the rf signals. At a given moment in time, the spatially modulated light that is incident on the photoconductive layer of the detector will generate photocarriers in proportion to the local intensity, and these carriers will drift with a velocity proportional to the applied bias voltage. Varying the applied bias voltage in the photoconductor changes this drift velocity, and a photocurrent resonance peak occurs when the induced electron drift velocity equals the fringe velocity of the moving interference pattern. For the desired phased-array signal  $s_n(t')$  diffracted by the grating, the interferometric fringes will all move at the magnified acoustic velocity, which can be set equal to the velocity of the photogenerated carriers by fine tuning the bias voltage. The unwanted but unavoidable diffractions of the jammers off the sidelobes of the photorefractive grating, however, will not have the necessary frequency–angle relationship to produce constant velocity moving fringes at the carrier and the drift velocity. Thus the jammers will be somewhat suppressed and washed out—both by the angular selectivity of the diffraction by the photorefractive crystal, and in the frequency domain by the temporal filtering associated with resonant detection of constant velocity interferometric fringes on the TFD.

The first two terms in Eq. (21) are unwanted dc terms and will contribute only to bias in the detector. The desired detected interference pattern, however, is moving at a velocity  $v_D = m_1 m_2 v_A$ , the acoustic velocity of the AOD scaled by the overall magnification of the lens systems  $L_1$  and  $L_2$ . If the AOD has a time–bandwidth product  $M$ , with spatial resolution  $\Delta x_2$ , then the TFD will detect the moving interference pattern over a time  $T_D = M \Delta x_2 / (m_1 m_2 v_A) = M \Delta x_2 / v_D$  with a responsivity  $R$ . Assuming that the magnification has scaled the velocity and been fine

tuned with the bias voltage across the device to be synchronous with the photogenerated carriers, the final output is

$$o(t) = R \int_{-T_D/2}^{T_D/2} \int_{-\infty}^t I(x_2, t') \delta \left[ (t' - t) - \frac{x_2}{v_D} + t_{r_2} \right] \times dt' dx_2 / v_D = R \int_{-T_D/2}^{T_D/2} I(x_2, t + \tau_x - t_{r_2}) d\tau_x, \quad (22)$$

where  $t_{r_2}$  is another reference delay that allows the TFD to be centered within the optical system and the limits of integration to remain causal, and  $\tau_x = x_2/v_D$ . When we substitute this expression into the detected signal of interest, then

$$o(t) = R \kappa_2 \int_{-T_D/2}^{T_D/2} \sum_{n=1}^N \tilde{s}_n(t - t_n + \tau_x - t_{r_2}) \times \int_{-\infty}^{t + \tau_x - t_{r_2}} \tilde{f}(t_0 - \tau_x - t_{r_1}) \tilde{s}_n^*(t_0 - t_n - T) dt_0 d\tau_x = R \kappa_2 \int_{-T_D/2}^{T_D/2} \sum_{n=1}^N \tilde{s}_n(t - t_n + \tau_x - t_{r_2}) \times \int_{-\infty}^t \tilde{f}[t_1 - (t_{r_1} + t_{r_2})] \tilde{s}_n^*(t_1 - t_n - T + \tau_x - t_{r_2}) \times dt_1 d\tau_x. \quad (23)$$

The feedback signal  $\tilde{f}[t_1 - (t_{r_1} + t_{r_2})]$  contains the output signal with a feedback time delay  $t_f$ , which when combined with the reference delays  $(t_{r_1} + t_{r_2})$ , provides the total round-trip time delay  $T = t_f + (t_{r_1} + t_{r_2})$ . The reference delays were used to center the AOD and the TFD within the optical system, and  $(t_{r_1} + t_{r_2})$  represents the total fixed time delay that is incurred by each of the signals propagating through the two TDL's. Expanding the feedback signal into its desired and output signal components,

$$\tilde{o}(t) = R \kappa_2 \int_{-T_D/2}^{T_D/2} \sum_{n=1}^N \tilde{s}_n(t - t_n + \tau_x - t_{r_2}) \times \int_{-\infty}^t g_2[\tilde{d}(t_1 - t_d) - g_1 \tilde{o}(t_1 - T)] \times \tilde{s}_n^*(t_1 - t_n - T + \tau_x - t_{r_2}) dt_1 d\tau_x = R \kappa_2 \int_{-T_D/2}^{T_D/2} \sum_{n=1}^N \tilde{s}_n(t - t_n + \tau_x - t_{r_2}) \times \int_{-\infty}^{t-T} g_2\{\tilde{d}[t_2 + (T - t_d)] - g_1 \tilde{o}(t_2)\} \times \tilde{s}_n^*(t_2 - t_n + \tau_x - t_{r_2}) dt_2 d\tau_x. \quad (24)$$

Equation (24) shows that, with the total round-trip delay  $T$  appropriately incorporated into both the feedback signal and the writing signal from the phased array, a temporal equation is created that is identical to that of Eq. (8). A cross correlation is formed between fixed delayed versions of the signal from the antenna array and a delayed version of the feedback signal, which is then convolved with the instantaneous signals from the array to provide the final output  $\tilde{o}(t)$ . Since  $\tilde{o}(t)$  appears on both sides of this integral equation, it is difficult to solve in the time domain; hence we will subsequently transform to a Fourier-domain representation.

#### H. Frequency-Domain Analysis

Equation (24) represents the adaptation of the output to an arbitrary signal environment with an arbitrary number of jamming signals present, where  $\tilde{s}_n(t) = \tilde{r}(t - nt_p) + \sum_j \tilde{j}_j(t - nt_j)$ . The steady-state solution of this equation can be derived by transformation to the frequency domain and by algebraic manipulation of the spectra to solve for  $\tilde{O}(f)$ . At steady state with  $t \gg T$ , the output signal is a spatiotemporal convolution of the signal from the phased array with the cross-correlation function of the delayed feedback signal with the delayed version of the phased-array signal. When transformed to the temporal Fourier domain, Eq. (24) becomes

$$\tilde{O}(f) = R\kappa_2 \sum_n \tilde{S}_n(f) g_2 \{ \tilde{D}(f) \exp[i2\pi f(T - t_d)] - g_1 \tilde{O}(f) \} \tilde{S}_n^*(-f) * T_D \text{sinc}(T_D f), \quad (25)$$

where  $*$  denotes a convolution. Solving for the frequency-domain output  $\tilde{O}(f)$ ,

$$\tilde{O}(f) = \frac{g_2 R\kappa_2 \sum_n |\tilde{S}_n(f)|^2 \tilde{D}(f) \exp[i2\pi f(T - t_d)] * T_D \text{sinc}(T_D f)}{1 + g_1 g_2 R\kappa_2 \sum_n |\tilde{S}_n(f)|^2 * T_D \text{sinc}(T_D f)}, \quad (26)$$

where the  $\exp[i2\pi f(T - t_d)]$  phase term denotes the arbitrary timing necessary to ensure that the cross correlation between the desired signal and the signals from the phased array occurs within the photorefractive crystal. Noting that the Fourier transform of the input signal  $\tilde{s}_n(t)$  is  $\tilde{S}_n(f) = \tilde{R}(f) \exp(-i2\pi n t_p) + \sum_j \tilde{J}_j(f) \exp(-i2\pi n t_j)$  and is dominated by the jammers, the term in the denominator will simplify to the sum of the powers of the jamming signals present  $\sum_n |\sum_j \tilde{J}_j(f)|^2 = \sum_n \sum_j |\tilde{J}_j(f)|^2$ , since the jammers are assumed to be mutually independent. This is a valid approximation for many signal environments, since typically the signal of interest is buried beneath the noise floor, whereas the jamming signal may be as large as 30–60 dB above the noise. The frequency-domain sinc function represents the limitation of temporal degrees of freedom

but can be approximated as a delta function when  $T_D$  is much greater than the correlation time of the desired signal,<sup>38</sup> yielding

$$\tilde{O}(f) = \frac{\frac{g}{g_1} \sum_n \tilde{S}_n(f) \{ \tilde{S}_n^*(-f) \tilde{D}(f) \exp[i2\pi f(T - t_d)] \}}{1 + g \sum_n \sum_j |\tilde{J}_j(f)|^2}, \quad (27)$$

where  $g = g_1 g_2 R\kappa_2 T_D$  is the net gain around the loop.

Spatial Fourier transformation can now be used to illustrate the spatiotemporal frequency response of the system. Noting that  $\tilde{S}_n(f) = \sum_l \tilde{S}(k_l, f) \exp(ik_l n d)$ , and that  $\tilde{S}(k_l, f) = \sum_n \tilde{S}_n(f) \exp(-ik_l n d)$ , where  $k_l = 2\pi l / (Nd)$  (for  $l = -N/2, \dots, N/2$ ), and expanding the detected signal into its constituent signal and jammer components at their respective angles of arrival,  $\tilde{S}_n(f) = \tilde{R}(f) \exp[i2\pi f/c \sin(\theta_r) n d] + \sum_j \tilde{J}_j(f) \exp[i2\pi f/c \sin(\theta_j) n d]$  since  $t_p = f/c d \sin \theta_r$ , and  $t_j = f/c d \sin \theta_j$ , yields

$$\tilde{S}(k_l, f) = \left[ \tilde{R}(f) \delta\left(k_l - \frac{f}{c} \sin \theta_r\right) + \sum_j \tilde{J}_j(f) \times \delta\left(k_l - \frac{f}{c} \sin \theta_j\right) \right] * Nd \text{sinc}(Nd k_l). \quad (28)$$

Thus broadband signals lie on a tilted locus in spatiotemporal Fourier space (pivoting through  $k_l = 0$ ,  $f = 0$ ) and are blurred by the finite array size.

The detected signal of interest  $\tilde{R}(f) \delta(k_l - f/c \sin \theta_r)$  correlates against the desired signal  $\tilde{D}(f)$ , and can be separated into a known component  $\alpha \tilde{D}(f)$  that correlates perfectly with  $\tilde{D}(f)$ , and an unknown component  $\alpha' \tilde{D}'(f)$  that is independent of it. This allows for further simplification of the output, since only the part that is correlated with the desired signal will write a grating within the photorefractive crystal. Since the desired signal is also uncorrelated to any of the jamming signals, the output takes on the form

$$\tilde{O}(f) = \sum_{k_l} \tilde{S}(k_l, f) \times \frac{\frac{g}{g_1} \alpha |\tilde{D}(f)|^2 \exp[i2\pi f(T - t_d)] \delta\left(k_l - \frac{f}{c} \sin \theta_r\right) * b(k_l, f)}{1 + g \sum_{k_l} \sum_j |\tilde{J}_j(f)|^2 \delta\left(k_l - \frac{f}{c} \sin \theta_j\right) * b(k_l, f)}, \quad (29)$$

where  $b(k_l, f) = T_d \text{sinc}(T_d f) Nd \text{sinc}(Nd k_l)$  denotes the total blur function. The linear adaptive-array output-frequency response is given by a weighted signal spatiotemporal frequency spectrum that is summed across all spatial frequencies,

$$\tilde{O}(f) = \sum_{k_l} \tilde{S}(k_l, f) \tilde{T}(k_l, f), \quad (30)$$

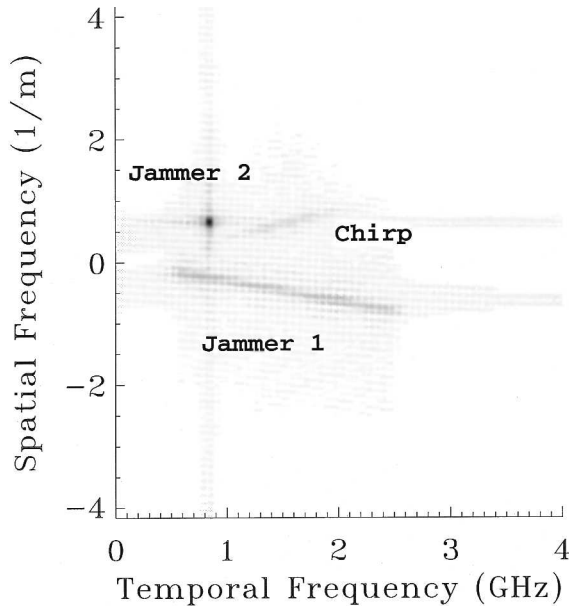


Fig. 8. Spatiotemporal Fourier space representation of the input signals used in the computer simulation of the BEAMTAP algorithm, which were selected to test the system's jammer-nulling capacity over a diversified signal environment. The desired signal is a broadband Gaussian chirp (1.2–1.8 GHz) at 0.25 rad AOA. Jammer 1 is broadband filtered Gaussian noise (0.5–2.5 GHz) at  $-0.2$  rad AOA, and jammer 2 is a single-frequency 0.8 GHz at 0.5 rad AOA sine wave, each of which are 30 dB stronger than the signal of interest.

and this allows the steady-state spatiotemporal transfer function of the BEAMTAP processor to be defined as

$$\tilde{T}(k_l, f) = \frac{\frac{g}{g_1} \alpha |\tilde{D}(f)|^2 \exp[i2\pi f(T - t_d)] \delta\left(k_l - \frac{f}{c} \sin \theta_r\right) * b(k_l, f)}{1 + g \sum_{k_l} \sum_j |\tilde{J}_j(f)|^2 \delta\left(k_l - \frac{f}{c} \sin \theta_j\right) * b(k_l, f)} \quad (31)$$

The maximum array sensitivity is along the tilted locus in spatiotemporal frequency space corresponding to the desired signal AOA, with a bandwidth tuned to the power spectrum of the steering signal  $|D(f)|^2$  (actually flattened by the LMS dynamics). This output achieved the full array gain of  $Nd$ , since the beam-forming operation has a linear phase that time delays the arriving signal to time align it with the known reference signal. Jammer nulling is accomplished by an inverse filter (the denominator) that acts as a power nuller to any jamming signals present in the signal environment at their respective angles of arrival [denoted by the  $\delta(k_l - f/c \sin \theta_j)$  term] and frequency spectrums. The total null depth of the processor is limited by the effective loop gain  $g$ , and the available null depth is distributed among the number of jamming signals present.<sup>29</sup> The grating within the photorefractive processor will

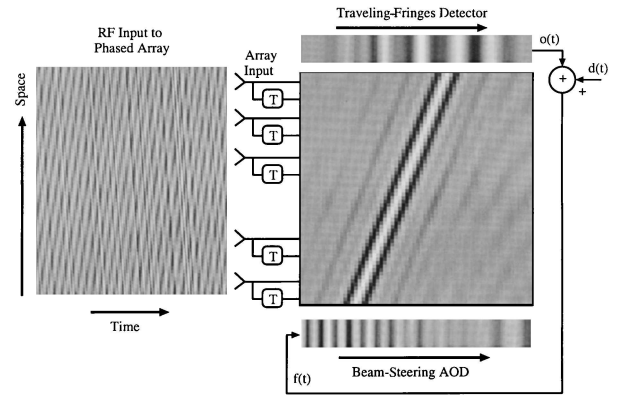


Fig. 9. Diagram illustrating the simulation of the BEAMTAP architecture. The input signal is represented by the array of time histories shown on the left-hand side. At every time step an instantaneous slice of the input is detected by the antenna arrays and is propagated through the adaptive weight matrix (center of figure). The product of the input vector with the weight matrix is diffracted vertically and detected and accumulated on the scrolling detector (top of figure). The output  $o(t)$  is subtracted from the desired signal  $d(t)$ , generating the feedback signal  $f(t)$ , which is fed through the scrolling delay line (bottom of figure). An outer product between the scrolling feedback signal and a delayed version of the input is used to adapt the weights, producing the resulting tilted cross-correlation slice seen in the weight matrix in the center of the figure at steady state.

respond more quickly to higher-power jamming signals to create a greater null depth, whereas smaller-power jamming signals will not be nulled as deeply, or as quickly (although the jammers' final power will be the same after adaptation). As in all LMS-based power nulling processors, when the signal of interest

is strong, its corresponding output amplitude will be clamped to the signal power of the desired signal, since the  $\sum_{k_l} |\tilde{S}(k_l, f)|^2$  term in the denominator of the transfer function will no longer be dominated by the sum of the power of the jamming signals.

Beam steering is driven by the known component  $\alpha \tilde{d}(t)$  of the desired signal detected at the array  $r(t) = \alpha \tilde{d}(t) + \alpha' \tilde{d}'(t)$ , which can be either time multiplexed or code multiplexed with the spectrally overlapping unknown desired signal  $\alpha' \tilde{d}'(t)$ . The TFD output contains both  $\tilde{d}(t)$  and  $\tilde{d}'(t)$  weighted proportionally to  $\alpha$  and  $\alpha'$ , respectively, since they are broadcast by a single transmitter and arrive on the array with identical phase fronts. At steady state, the amplitude of the known component at the differencing node adaptively adjusts to a nearly exact match of the known reference signal; thus just after the differencing node, the known component is canceled, and the

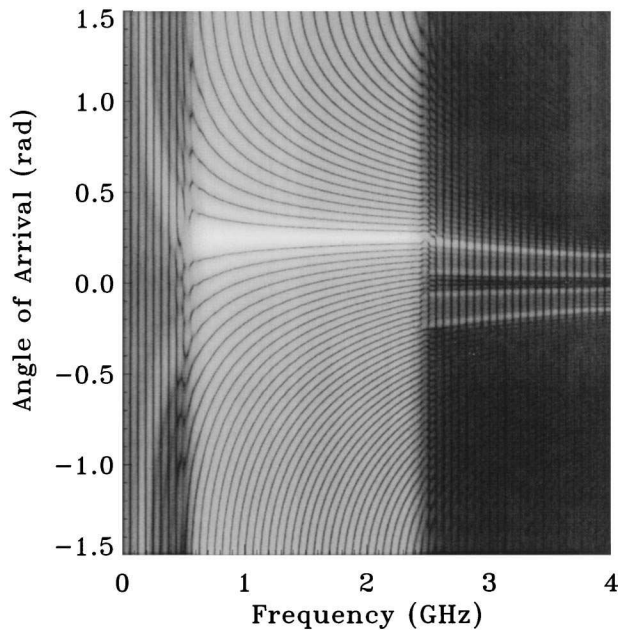


Fig. 10. AOA versus frequency receptivity pattern that develops after adaptation when only the desired signal is present at the input. Note that the main lobe at 0.25 rad AOA does not vary its position with frequency (although its width does change) as it spans the entire input signal bandwidth—thereby demonstrating squint-free TTD beam forming.

unknown desired signal  $\alpha \tilde{D}'(f)$  remains detected with the full array gain and all of the jammers are optimally extinguished.

#### I. BEAMTAP System Simulations

We simulated the BEAMTAP algorithm to demonstrate its operation for broadband squint-free beam forming and jammer nulling and to verify the spatiotemporal frequency-domain transfer function formalism. Figure 8 characterizes the input signals in spatiotemporal Fourier space with transverse spatial frequency along the vertical axis and a single-sided temporal frequency along the horizontal axis. The desired signal is a broadband Gaussian apodized chirp whose  $1/e$  spectrum spans the frequency range from 1.1 to 1.9 GHz. Its AOA is set at 0.25 rad, and it falls on a tilted locus in spatiotemporal frequency space. Jammer 1 is a broadband filtered Gaussian white-noise signal, spanning the frequency range from 0.5 to 2.5 GHz, with an AOA of  $-0.2$  rad. Jammer 2 is a narrow-band sine wave, set at a frequency of 0.8 GHz and with an AOA of 0.5 rad. Jammer 2 is selected such that it lies on the maximum of the first sidelobe of the receptivity pattern of the chirp when beam forming is performed without jammers. In the simulations presented here, the power in each jammer is 1000 times stronger than the power in the desired signal. However, the power of all signals was normalized in Fig. 8 for illustrative purposes to make all the signals visible.

The diagram shown in Fig. 9 illustrates the various facets of the simulation. The leftmost figure shows

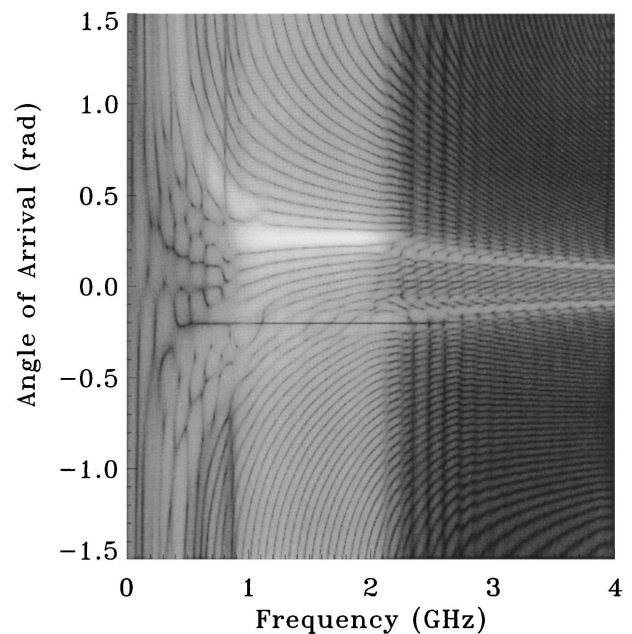


Fig. 11. AOA versus frequency receptivity pattern after adaptation when the desired signal and strong jammers are both present at the input—demonstrating squint-free jammer suppression with deep nulls. Note the extremely narrow constant angle squint-free null at the angle of the broadband jammer ( $-0.2$  rad) over its full bandwidth, a narrow-band null at 0.5 rad and 800 MHz with deep sidelobe nulls, and a slight reduction in the bandwidth of the system response to the desired signal in comparison with Fig. 10 (although more than the full  $1/e$  bandwidth of the signal is still uniformly detected).

the spatiotemporal rf field amplitude detected by the array antennas sampled at 125 ps (i.e., with a frequency  $f_s = 8$  GHz) along the horizontal time axis and spatially sampled by the 64 antenna elements along the vertical axis. Note that only the jammers are visible, since they are much stronger than the signal. The final weight values after adaptation for 300  $\mu$ s with a net loop gain of 1 are shown in the center of this figure. Note also that, even though the signal is totally buried by the jammers, the dominant feature that builds up in the weight matrix is the tilted stripe that results from the correlation between the desired component of the feedback signal  $f(t) = d(t) - o(t)$  (the difference between the desired chirp signal and the output) and the input signals  $s_n(t)$  (chirp and jammers) whose tilt is an indication of the AOA of the desired signal. Weak sidelobes seen in the weight matrix are due to a cross correlation between the signal and the jammers and are responsible for the manipulation of the antenna nulls to point toward any undesired jammers. The instantaneous input signal vector from the array is multiplied (e.g., diffracted vertically) by this weight matrix to transform array element positions into topologically ordered spatial positions arranged with linear time delays at the velocity of the TFD; detection on the TFD thereby compensates for the unknown time delays to each

antenna element of the desired signal. The diffracted signal is deflected vertically where it is detected and accumulated in the scrolling detector array, which in this simulation was shifting at a sampled rate of 8 GHz. The upper part of the figure shows the contents of the TFD at this instant, illustrating the accumulation of the light diffracted by the photorefractive weights, which generates the system output  $o(t)$  after propagating fully across the detector aperture. The lower part of the figure shows the contents of the scrolling input modulator (AOD) at this instant in time. An outer product (e.g., holographic interference) between this signal in the AOD and a delayed version of the input signal is used to adapt the weights. This simulation used an array with 64 antenna elements and 64 taps in the delay line.

Figures 10 and 11 show the receptivity pattern as a function of AOA and temporal frequency of the system for two different cases, first with only the signal present in the environment, and then in the presence of the strong jammers as well. The receptivity patterns were produced by simulation of narrow Gaussian pulses incident on the phased array coming from different AOA's, according to the expression  $T(\theta, f) = O(f)/G(f)|_{g_n(\theta, t)}$ , where  $G(f)$  represents the spectrum of the incident Gaussian pulse,  $g_n(\theta, t) = \exp[-(t - nd/c \sin \theta)^2/\Delta^2]$  represents the Gaussian pulse detected by each antenna element, and  $\Delta$  represents the  $1/e$  pulse width. Each pulse is propagated through the BEAMTAP system (with frozen weights) to provide the corresponding output. The output is Fourier transformed and is then divided by the spectrum of the initial Gaussian pulse, providing us with the transfer function for a given AOA. Repeating this process over several AOA's gives the final transfer function as a function of  $\theta$  and  $f$  in terms of the weights

$$T(\theta, f) = \sum_{n=1}^N \sum_{\tau=0}^{M-1} W_{\tau n} \exp \left[ -i2\pi f \left( t_s \tau + n \frac{d}{c} \sin \theta \right) \right], \quad (32)$$

where  $t_s$  is the sampling period. This function is a coordinate-transformed version of the spatiotemporal transfer function derived in Eq. (31), where the tilted loci in the spatiotemporal frequency representation are mapped onto the orthogonal sampling of the AOA-temporal frequency representation.

In Fig. 10, beam forming is performed only with the desired repetitive chirp in the input, without the jammers. Note the strong response in the direction of the desired signal (0.25 rad), over almost the entire chirp bandwidth (0.5 to 2.5 GHz), spatially blurred by the angular resolvability of the finite rectangular aperture of the array, which of course varies with frequency. It is interesting to note that, even though the chirp has a Gaussian window, the system transfer function is almost flat over the full bandwidth of the signal. This is explained by the fact that the system adapts to produce an output that resembles

the desired signal as closely as possible. Since both the input and the desired signals are Gaussian chirps, it is to be expected that the system response should be flat over the entire signal bandwidth until noise or jammers start to dominate the signal. Also note that maximum receptivity describes an untilted line at a constant unsquinted angle that is characteristic of a TTD system. However, the mainlobe width does vary with frequency as do the positions of the sidelobes and nulls. This is to be expected, since adaptation in the presence of signals and antenna noise has optimized the response of the main lobe only.

In Fig. 11, both the signals and the jammers are present in the signal environment, so beam forming and jammer nulling are performed simultaneously. Note the changes compared with Fig. 10. The main lobe's bandwidth has been slightly reduced, but it still covers the full  $1/e$  spectrum of the signal (1.1 to 1.9 GHz). Part of this reduction is explained by the presence of narrow-band jammer 2 at 0.8 GHz, on the first sidelobe of the main beam. Since the spatial sidelobe of this jammer extended onto the main beam and throughout its sidelobes, an improved error performance occurs by production of a null in that frequency, which covers a wide span of AOA's without any detrimental effect on the received signal. The wideband jammer 1 produced a long and thin null, located exactly at its AOA ( $-0.2$  rads), spanning its complete bandwidth (from 0.5 to 2.5 GHz) without any squint of the null, and a width that is significantly less than then main beam of the array. Both jammers were nulled to a depth of 45 dB with respect to the power of the detected signal of interest.

#### 4. Conclusion

We have presented, analyzed, and simulated an approach to broadband beam forming called BEAMTAP (broadband and efficient adaptive method for true-time-delay array processing) that reduces the number of TDL's required for time-domain adaptive beam forming of a broadband  $N$ -element antenna from the conventional value of  $N$  TDL's to only 2. For large arrays, this enables a dramatic hardware savings that will allow for the implementation of broadband adaptive phased arrays in sizes that were previously impractical. The rf photonic implementation of this BEAMTAP algorithm is ideally matched to the strengths of optical phased-array processing systems. We have presented an optical architecture based on this new hardware-efficient adaptive algorithm that uses a fiber-remoted coherent phased array, a photorefractive crystal, AOD, and a synchronously scanning TFD, whose electronic output represents the adaptively beam-steered and jammer-nulled output. Simulations were presented that verified this operation for broadband desired signals in the presence of narrow-band and broadband jammers.

We gratefully acknowledge the support and the direction of William Miceli of the Office of Naval Research and the Office of the Secretary of Defense,

Director of Defense Research and Engineering, through Multidisciplinary University Research Initiative program grant N00014-97-1-1006; the insight of Anthony Sarto of Ball Aerospace; and our collaborations with Daniel Dolfi of Thomson-CSF. In addition, we fondly remember the guidance and assistance by the late Brian Hendrickson of Rome Labs.

## References

1. D. Psaltis and J. Hong, "Adaptive acoustooptic filter," *Appl. Opt.* **23**, 3475–3481 (1984).
2. W. Ng, A. A. Walston, G. L. Tangonan, J. J. Lee, I. L. Newberg, and N. Bernstein, "The first demonstration of an optically steered microwave phased array antenna using true-time-delay," *J. Lightwave Technol.* **9**, 1124–1131 (1991).
3. R. D. Esman, M. Y. Frankel, J. L. Dexter, L. Goldberg, M. G. Parent, D. Stilwell, and D. G. Cooper, "Fiber-optic prism true time-delay antenna feed," *IEEE Photonics Technol. Lett.* **5**, 1347–1349 (1993).
4. P. J. Matthews, M. Y. Frankel, and R. D. Esman, "A wide-band fiber-optic true-time-steered array receiver capable of multiple independent simultaneous beams," *IEEE Photonics Technol. Lett.* **10**, 722–724 (1998).
5. D. Casasent, "Optical processing for adaptive phased-array radar," *IEE Proc. F.* **127**, 278–284 (1980).
6. D. Voskresenskii, A. Grinev, and E. Voronin, *Electrooptical Arrays* (Springer-Verlag, Berlin, 1989).
7. D. Psaltis and J. Hong, "Adaptive acoustooptic processor," in *Analog Optical Processing and Computing*, H. J. Caulfield, ed., Proc. SPIE **519**, 62–68 (1984).
8. S.-C. Lin, J. Hong, R. Boughton, and D. Psaltis, "Broadband beamforming via acousto-optics," in *Advances in Optical Information Processing III*, D. R. Pape, ed., Proc. SPIE **936**, 152–162 (1988).
9. J. H. Hong, "Broadband phased array beamforming," in *Optical Technology for Microwave Applications IV*, S.-K. Yao, ed., Proc. SPIE **1102**, 134–141 (1989).
10. W. A. Penn, R. Wasiewicz, and R. Iodice, "Optical adaptive multipath canceller for surveillance radar," in *Optoelectronic Signal Processing for Phased-Array Antennas II*, B. M. Hendrickson and G. A. Koepf, eds., Proc. SPIE **1217**, 151–160 (1990).
11. R. M. Montgomery, "Acousto-optic/photorefractive processor for adaptive antenna arrays," in *Optoelectronic Signal Processing for Phased-Array Antennas II*, B. M. Hendrickson and G. A. Koepf, eds., Proc. SPIE **1217**, 207–217 (1990).
12. D. R. Pape, "Multichannel Bragg cells: design, performance, and applications," *Opt. Eng.* **31**, 2148–2158 (1992).
13. J. J. Lee, R. Y. Loo, S. Livingston, V. I. Jones, J. B. Lewis, H.-W. Yen, G. L. Tangonan, and M. Wechsberg, "Photonic wideband array antennas," *IEEE Trans. Antennas Propag.* **43**, 966–982 (1995).
14. A. P. Goutzoulis, D. K. Davies, and J. M. Zomp, "Hybrid electronic fiber optic wavelength-multiplexed system for true time-delay steering of phased array antennas," *Opt. Eng.* **31**, 2312–2322 (1992).
15. R. Soref, "Optical dispersion technique for time-delay beam steering," *Appl. Opt.* **31**, 7395–7397 (1992).
16. L. J. Lembo, T. Holcomb, M. Wickham, P. Wissemann, and J. C. Brock, "Low-loss fiber optic time-delay element for phased-array antennas," in *Optoelectronic Signal Processing for Phased-Array Antennas IV*, B. M. Hendrickson, ed., Proc. SPIE **2155**, 13–23 (1994).
17. R. T. Weverka, K. Wagner, and A. Sarto, "Photorefractive processing for large adaptive phased arrays," *Appl. Opt.* **35**, 1344–1366 (1996).
18. K. Wagner, S. Kraut, L. Griffiths, S. Weaver, R. T. Weverka, and A. W. Sarto, "Efficient true-time-delay adaptive-array processing," in *Radar Processing, Technology, and Applications*, W. J. Miceli, ed., Proc. SPIE **2845**, 287–300 (1996).
19. M. A. Copeland, D. Roy, J. D. E. Beynon, and F. Y. K. Dea, "An optical CCD convolver," *IEEE Trans. Electron Devices* **ED-23**, 152–155 (1976).
20. K. Bromley, A. C. H. Louie, R. D. Martin, J. J. Symanski, T. E. Keenan, and M. A. Monahan, "Electro-optical signal processing module," in *Real-Time Signal Processing II*, T. F. Tau, ed., Proc. SPIE **180**, 107–113 (1979).
21. T. Merlet, D. Dolfi, and J.-P. Huignard, "A traveling fringes photodetector for microwave signals," *IEEE J. Quantum Electron.* **32**, 778–783 (1996).
22. D. Dolfi, T. Merlet, A. Mestreau, and J.-P. Huignard, "Photodetector for microwave signals based on the synchronous drift of photogenerated carriers with a moving interference pattern," *Appl. Phys. Lett.* **65**, 2931–2933 (1994).
23. B. Widrow and S. D. Stearns, *Adaptive Signal Processing* (Prentice-Hall, Englewood Cliffs, N.J., 1985).
24. B. Widrow, P. E. Mantey, L. J. Griffiths, and B. B. Goode, "Adaptive antenna systems," *Proc. IEEE* **55**, 2143–2161 (1967).
25. A. W. Sarto, R. T. Weverka, and K. Wagner, "Beam-steering and jammer nulling photorefractive phased-array radar processor," in *Optoelectronic Signal Processing for Phased-Array Antennas IV*, B. M. Hendrickson, ed., Proc. SPIE **2155**, 378–388 (1994).
26. A. W. Sarto, K. H. Wagner, R. T. Weverka, S. Blair, and S. Weaver, "Photorefractive phased-array antenna beamforming processor," in *Radar Processing, Technology, and Applications*, W. J. Miceli, ed., Proc. SPIE **2845**, 307–318 (1996).
27. R. T. Compton, *Adaptive Antennas* (Prentice-Hall, Englewood Cliffs, N.J., 1988).
28. M. A. G. Abushagur and H. J. Caulfield, "Speed and convergence of bimodal optical computers," *Opt. Eng.* **26**, 22–27 (1987).
29. A. W. Sarto, "Adaptive phased-array radar signal processing array using photoreactive crystals," Ph.D. dissertation (University of Colorado, Boulder, Colo., 1996).
30. R. T. Compton, "The effect of differential time delays in the LMS feedback loop," *IEEE Trans. Aerosp. Electron. Syst.* **AES-17**, 222–228 (1981).
31. A. W. Sarto, K. H. Wagner, R. T. Weverka, S. Weaver, and E. K. Walge, "Wide angular aperture holograms in photorefractive crystals by the use of orthogonally polarized write and read beams," *Appl. Opt.* **35**, 5765–5775 (1996).
32. A. Kiruluta, G. Kriehn, P. E. X. Silveira, S. Weaver, and K. H. Wagner, "Operator notational analysis of a photorefractive phased array processor," in *Digest of Topical Meeting on Optics in Computing*, Y. Fainman, ed. (Optical Society of America, Washington, D.C., 1999), 170–172.
33. D. Z. Anderson and J. Feinberg, "Optical novelty filters," *IEEE J. Quantum Electron.* **25**, 635–647 (1989).
34. A. A. Zozulya and D. Z. Anderson, "Spatial structure of light and a nonlinear refractive index generated by fanning in photorefractive media," *Phys. Rev. A* **52**, 878–881 (1995).
35. Y. Fainman, E. Klanchnik, and S. H. Lee, "Optimal coherent image amplification by two-wave coupling in photorefractive BaTiO<sub>3</sub>," *Opt. Eng.* **25**, 228–234 (1986).
36. M. Y. Frankel and R. D. Esman, "Optical single-side-band suppressed-carrier modulator for wide-band signal-processing," *J. Lightwave Technol.* **16**, 859–863 (1998).
37. M. H. Garrett, J. Y. Chang, H. P. Jenssen, and C. Warde, "High photorefractive sensitivity in an *n*-type 45°-cut BaTiO<sub>3</sub> crystal," *Opt. Lett.* **17**, 103–105 (1992).
38. A. VanderLugt, *Optical Signal Processing* (Wiley, New York, 1992).